Università degli Studi di Padova

DIPARTIMENTO DI FISICA E ASTRONOMIA GALILEO GALILEI
Master Degree in Astronomy

MASTER THESIS

Investigating rotation in young massive star clusters by means of hydro-dynamical and direct N-Body simulations

Candidate
Ugo Niccolò Di Carlo

Supervisor
Prof. Giampaolo Piotto

Co-Supervisor
Dr. Michela Mapelli

Anno Accademico 2016/2017

“Mannaggia.”

UNDC

Contents

Abstract

One of the main open questions of star formation is the process of star clusters aggregation. In my thesis I investigate the kinematical features of embedded star clusters through hydrodynamical and N-body simulations. In particular I focus on the onset of rotation. I started from smoothed-particle-hydrodynamics simulations of turbulence-supported molecular clouds with masses ranging from $10000\,\mathrm{M}_\odot$ to $200000\,\mathrm{M}_\odot$. In each simulated cloud a star cluster forms by hierarchical assembly of several sub-clumps; during this process torque is exerted on the parent gas and the stellar component because they accrete on the main cluster structure with non-zero angular momentum. This angular momentum is transferred to the main cluster, which acquires significant rotation.

I study the dynamical evolution of the cluster that forms in each cloud using direct summation N-body codes, to see how rotation and ellipticity evolve through time.

My simulated star clusters start with large ellipticity ($\epsilon \sim 0.7$ at $t = 3\,\mathrm{Myr}$) and with a rotational velocity $v_{\mathrm{rot}} \sim 5\,\mathrm{km\ s}^{-1}$. During their evolution they tend to become rounder ($\epsilon \sim 0.2$ at $t = 10\,\mathrm{Myr}$) and their rotation signature decreases because of two-body relaxation. Rotation is still apparent at $t = 20\,\mathrm{Myr}$, so it decreases on a surprisingly long timescale.

This result is a key test to probe the hierarchical formation scenario of star clusters, and might be useful to interpret the observed rotation signature in young massive star clusters (R136, Hénault-Brunet et al. 2012) and in old globular clusters (e.g. Bellazzini et al. 2012).

Chapter 1

Star Clusters

In this section I describe the general properties of star clusters (SCs) focusing on their formation, dynamics and the feature of rotation, which are the subjects of study of my thesis.

1.1 Star Clusters Overview

SCs are self-gravitating collisional systems made up of stars. It is generally assumed that all the stars of a SC form from the same molecular cloud in a single star-formation event, so that they have approximately the same age and chemical composition[1]. They are excellent laboratories to study stellar dynamics, stellar evolution, intermediate mass black holes and gravitational wave sources.

In order to better describe the properties of such systems I need to define some typical size-scales and time-scales.

1.1.1 Size-scales

Star clusters tend to be approximately spherical in space or circular on the sky, so it is useful to define some different radii to measure their size.

We call Lagrangian radius the distance from the center containing a specific fraction of the total mass of the cluster. The most frequently used Lagrangian radius is the half-mass radius r_{hm}, which is the radius containing 50% of the total mass of the cluster.

A similar radius mainly used by observers can be defined using specific fractions of projected luminosity of the cluster. In this case, the analogue of the half-mass radius is the half-light radius r_{hl}, sometimes also called effective radius.

The virial radius is defined as:

$$r_{\mathrm{vir}} = \frac{GM^2}{2\,|U|} \tag{1.1}$$

where M is the total mass of the cluster and U is the total potential energy. It is a theoretical definition used to determine sizes of systems without a sharp boundary.

The tidal radius r_t is the radius where the gravitational acceleration of the cluster equals the tidal acceleration of the parent galaxy; it roughly corresponds to the distance where the density of stars drops to a value comparable to the background.

---

[1] Except for the globular clusters which show the feature of multiple populations.

Finally, the core radius r_c has several definitions. Observers define it as the radius at which the surface brightness equals half of its central value. Theorists define it in two different ways. The first is:

$$r_c = \sqrt{\frac{3\left\langle v^2\right\rangle_0}{4\pi G\rho_0}} \tag{1.2}$$

where ρ_0 and $\left\langle v^2\right\rangle_0$ are the central density and velocity dispersion. This is roughly the distance at which the projected density drops by a factor of 2. The second is generally used for n-body simulations and it is a density-weighted radius:

$$r_c = \sqrt{\frac{\sum_i \rho_i^2 r_i^2}{\sum_i \rho_i^2}} \tag{1.3}$$

1.1.2 Time scales

There are two fundamental time scales concerning star clusters: the dynamical time scale $t_{\rm dyn}$ and the relaxation time scale $t_{\rm rel}$.
The dynamical time-scale is the time required for a typical particle to cross the system and it is the time on which the system estabilishes the dynamical equilibrium. It may be defined as:

$$t_{\rm dyn} = \frac{GM^{5/2}}{(-4E)^{3/2}}, \tag{1.4}$$

where E is the total energy of the cluster. Another definition for systems in virial equilibrium is:

$$t_{\rm dyn} = \left(\frac{GM}{r_{\rm vir}^3}\right)^{-1/2} \sim 2\times 10^4\, yr \left(\frac{M}{10^6\, M_\odot}\right)^{-1/2} \left(\frac{r_{\rm vir}}{1\,\rm pc}\right)^{3/2}. \tag{1.5}$$

The relaxation time scale is the time over which stars reach equilibrium through mutual gravitational interactions and lose memory of their initial velocities.
An expression for the local relaxation time is:

$$t_{\rm rl} = \frac{N}{8\ln N}\frac{R}{v}. \tag{1.6}$$

where N is the number of stars of the cluster, R is the size of the cluster and v is the typical velocity of the stars of the cluster. This process and a derivation of equation 1.6 will be described in Section 1.3.

1.1.3 Properties of cluster systems

In our universe we observe SCs in different environments and with very different charateristics; we divide them into three main categories. **Globular clusters** (GCs) are nearly spherical systems composed of $10^4 - 10^6$ population II low mass stars ($m \lesssim 1\,\rm M_\odot$). They do not contain gas and dust and their age is comparable to the age of the Universe ($t \sim 10^{10}\,\rm Gyr$). GCs are really dense and their core can reach densities of $\sim 10^4\,\rm M_\odot\,pc^{-3}$. They mainly reside in the halos of galaxies. Some GCs

Table 1.1: Comparison of fundamental parameters for star cluster families: open cluster (OC), globular cluster (GC), and young massive cluster (YMC). The values are intended to be indicative. The second column gives cluster age, followed by the turn-off mass, the total cluster mass, the virial radius, the core density, the metallicity, the location where these clusters are found, and the dynamical and relaxation time scales. Data from Portegies Zwart et al. (2010).

Cluster	Age [Gyr]	m_{to} [$M_\odot$]	M [$M_\odot$]	$r_{\rm vir}$ [pc]	ρ_c [$M_\odot/pc^3$]	Z [$Z_\odot$]	Location	$t_{\rm dyn}$ [Myr]	$t_{\rm rh}$ [Myr]
OC	$\lesssim 0.3$	$\lesssim 4$	$\lesssim 10^3$	1	$\lesssim 10^3$	~ 1	disk	~ 1	$\lesssim 100$
GC	$\gtrsim 10$	~ 0.8	$\gtrsim 10^5$	10	$\gtrsim 10^3$	< 1	halo	$\gtrsim 1$	$\gtrsim 1000$
YMC	$\lesssim 0.1$	$\gtrsim 5$	$\gtrsim 10^4$	1	$\gtrsim 10^3$	$\gtrsim 1$	disk	$\lesssim 1$	$\lesssim 100$

show the feature of multi-population: they contain several distinct populations of stars mainly distinguished by their chemical composition. Many aspects about GCs are unclear: their formation, the onset of multiple populations and their role in galactic evolution are still matter of debate. **Open Clusters** (OCs) are loosely bound systems made up of $10 - 10^4$ population I stars. They may still contain gas and they are younger and less dense than GCs ($\rho \lesssim 10^3\,\mathrm{M_\odot\,pc^{-3}}$). They reside in the disk of galaxies. Some of them are visible to the naked eye (e.g. Hyades in figure 1.1 or the Pleyades). **Young Massive Clusters** (YMCs) are very young ($t \lesssim 100\,\mathrm{Myr}$) systems composed of $10^3 - 10^5$ young stars which may still contain gas. They have smaller size than GCs but their densities are comparable. They reside in the disk of galaxies and being so young they have a much larger fraction of massive stars than other kinds of SCs; we know that some YMCs like R136 (figure 1.1) host some stars with masses larger than $150 M_\odot$.

Some fundamental parameters of these kinds of SCs, their aspect and their location in the Milky Way are reported in table 1.1 and in figures 1.1 and 1.2 for comparison.

YDSCs are the subject of study of my thesis, and in particular I investigate their formation and dynamics.

1.2 Formation of SCs

The process of star formation constitutes one of the main problems of modern astrophysics. No predictive theory of star formation exists: given certain initial conditions, e.g. the density and temperature distributions inside an interstellar cloud, it is not possible to predict with certainty the star formation efficiency and the resulting initial mass function. We rely mostly on observations to answer these important questions. Stars are often observed to form in clusters and it is therefore important to understand how such regions are assembled out of the diffuse medium. The regions in which stars form are called molecular clouds (MCs), and their properties eventually determine the characteristics of the star clusters they form. MCs are turbulent interstellar clouds almost entirely made up of hydrogen. Their temperatures and densities allow the formation of molecular hydrogen H_2. Typical molecular clouds have masses of the order of $10^5\,\mathrm{M_\odot}$, dimensions of $\sim 10\,\mathrm{pc}$, temperatures of $10 - 100\,\mathrm{K}$ and densities of

Figure 1.1: **Left**: HST image of the open cluster NGC265 in the Small Magellanic Cloud. The image is $\sim 25\,\mathrm{pc}$ per edge. **Center**: M4, a globular cluster in the Milky Way. It is one of the closest GCs to the Solar System, with an estimated age of 12.2 Gyr. Image from the MPG/ESO 2.2-metre telescope at ESO's La Silla Observatory. The image is $\sim 20\,\mathrm{pc}$ per edge. **Right**: an HST image of R136, a YMC near the center of the 30 doradus star forming region in the LMC. R136 has an estimated age of 1.5 Myr, shows the feature of rotation (Hénault-Brunet et al. (2012)) and contains many very massive stars. The image is $\sim 50\,\mathrm{pc}$ per edge.

$10 - 300\,\mathrm{molecules/cm^3}$. A certain fraction, about 1% of the cloud, is in the form of dust which makes the clouds very opaque to visual wavelengths (Fig. 1.3). Molecular hydrogen is difficult to detect by infrared and radio observations, so the molecule used to determine the presence of H_2 is carbon monoxide (CO) which is in a ratio of 1 : 10000 with H_2.

Locally, molecular clouds are subject to gravitational instabilities for masses larger than the Jeans mass:

$$\mathrm{M_{Jeans}} = 4 \times 10^4 \mathrm{M_\odot} \left(\frac{T}{100\,\mathrm{K}}\right)^{3/2} \left(\frac{n}{\mathrm{cm^{-3}}}\right)^{-1/2} \tag{1.7}$$

where n is the numerical molecular density of the cloud. For typical values of T and n in MCs, $\mathrm{M_{Jeans}} \sim 10^3 - 10^4\,\mathrm{M_\odot}$.

Gravitational instabilities may be triggered by perturbations (e.g. shockwaves created by nearby supernovae or collisions with other clouds). When a perturbation disturbs the hydrostatic equilibrium, part of the cloud begins to collapse under its self-gravity. The collapse happens over the free-fall timescale $t_{ff} \propto 1/\sqrt{G\rho}$, and since the densities involved are very low, this timescale is of the order of ~ 1 Myr. The cloud is transparent to far-infrared radiation and thus cools efficiently, so that the early stages of the collapse are isothermal. As the density of the collapsing cloud increases, its Jeans mass decreases by equation 1.7, so that the cloud starts to fragment into smaller pieces, each of which continues to fragment and collapse to finally form the stars that will make up the cluster.

After few Myr, the most massive stars explode as supernovae and inject energy into the embedded gas which eventually becomes gravitationally unbound from the cluster and dissolves. Gas loss removes potential energy from the cluster, which loses some stars or may completely dissolve (infant mortality).

Spectroscopical observations of MCs show that on average, the linewidths displayed are much greater than expected from thermal motions at temperatures of $10 - 20\,\mathrm{K}$.

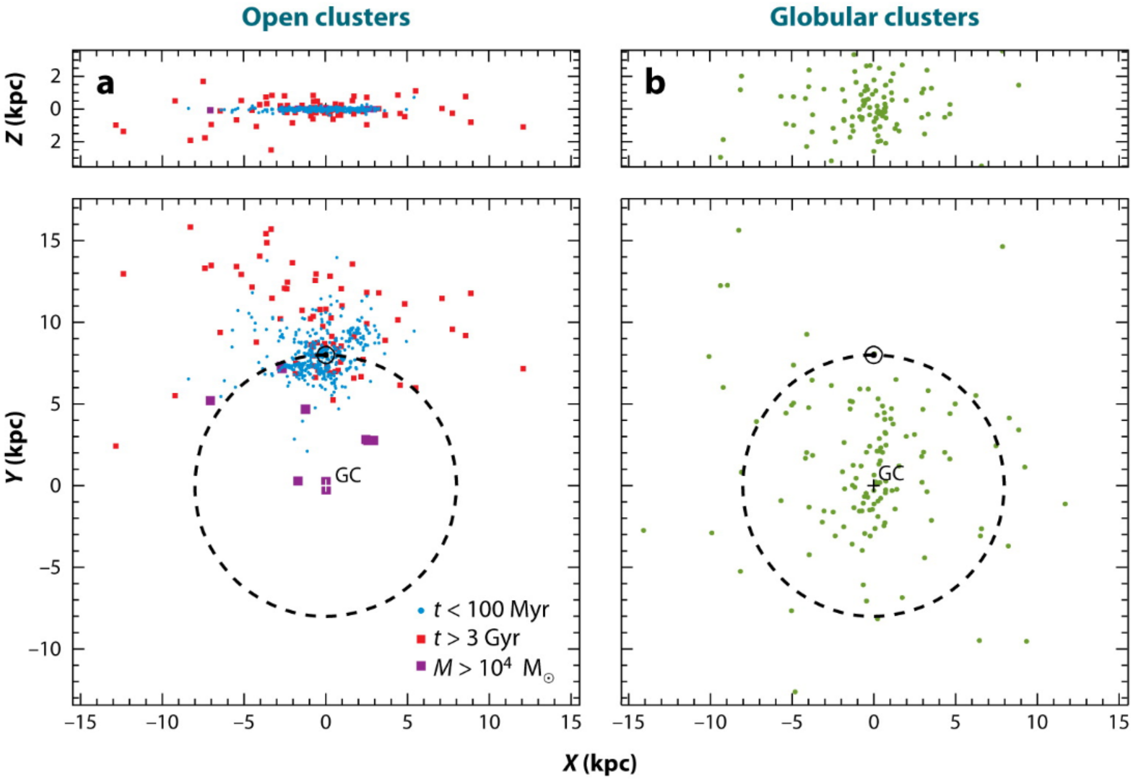

Figure 1.2: Distribution of star clusters in the Milky Way. In the top panels the Galaxy is seen edge-on, while on the bottom panels is seen face-on. The black dashed circle is the Sun's orbit around the Milky Way, the small black circle represents the Sun. Left: distribution of open clusters and young massive clusters (from the Dias 2012 catalogue). Right: distribution of globular clusters (from the Harris 1996 Catalogue). It's clear that GCs are spherically distributed around the center of the Galaxy while the other clusters are in the disk. The majority of OCs is near the Sun because of the extinction of dust which doesn't allow us to observe them over certain distances (from Portegies Zwart et al. (2010)).

In particular the observed linewidth is related to the size of the cloud by the Larson's scaling relation (Larson (1981)):

$$\sigma = 0.5 \left(\frac{L}{1.0\,\mathrm{pc}} \right)^{0.5} \mathrm{km\,s^{-1}}, \tag{1.8}$$

where L is the cloud size. These large non-thermal linewidths have been interpreted as indicating the presence of supersonic turbulence.
Turbulence of MCs plays a fundamental role in the formation of star clusters: on global scales it provides support preventing global collapse (Bertoldi & McKee (1992)), while at the same time it can promote local collapse creating an inhomegeneous filamentary structure which is characterized by large density contrasts (figure 1.4). Some of the high-density fluctuations exceed the Jeans mass and their collapse leads to the formation of clumps of stars.

At present, there are two main different scenarios for the formation of young star clusters from molecular clouds. **The monolithic collapse** (top-down) dictates the formation of a compact star cluster in a single star-formation episode. According to the **hierarchical assembly** (bottom-up) scenario, the formation happens through the merging of several less massive clumps of stars and gas which develop along the filaments. They fall onto each other while star formation is still in action and merge to form the final cluster near the junction of filments.
We still do not know how real clusters develop; the monolithic scenario is supported by the simulations of Banerjee & Kroupa (2015), while the simulations of Bonnell et al. (2003), Mapelli (2017) show formation through the hierarchical assembly.

1.3 Dynamics of SCs

The dynamical evolution of SCs is driven by many different processes acting together. We can distinguish two main stages in the evolution of a SC:

- The first Myrs in which star formation is still in action and the cluster still contains gas from its parent MC.
- The phase subsequent to gas evaporation in which purely stellar dynamical processes dominate.

The first phase is shorter, but is the most complex and less understood since it is a complex mix of gas dynamics, stellar dynamics, stellar evolution, and radiative transfer. Simulating both gas and stellar dynamics with high accuracy is difficult, so the majority of N-body simulations start from the second phase, using idealized initial conditions. The proper starting configuration for these simulations is largely a matter of conjecture.
After the gas is radiated away, the SC can be seen as a system of point masses (stars) which interact between each other by means of gravitational force. SCs are collisional systems, which means that interactions between particles are efficient with respect to the lifetime of the system. On the contrary, collisionless systems (e.g. galaxies) are systems where interactions are negligible, so that particles move under the influence of the gravitational field generated by a smooth mass distribution rather than a

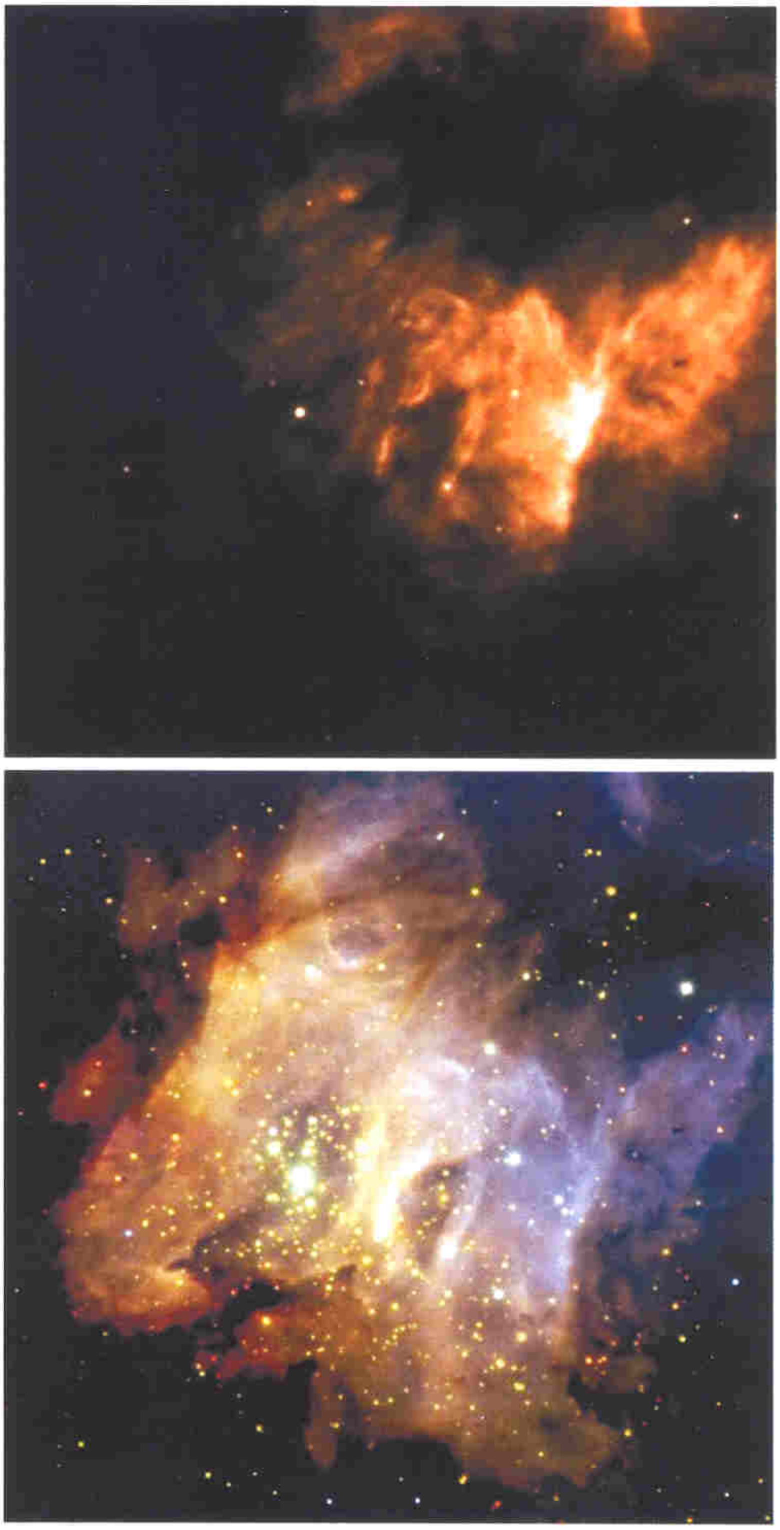

Figure 1.3: Optical (top) and Infrared (bottom) images of the RCW 38 region obtained with the ESO VLT. The infrared observations reveal a rich embedded cluster otherwise invisible at optical wavelengths. Figure from Lada & Lada (2003)

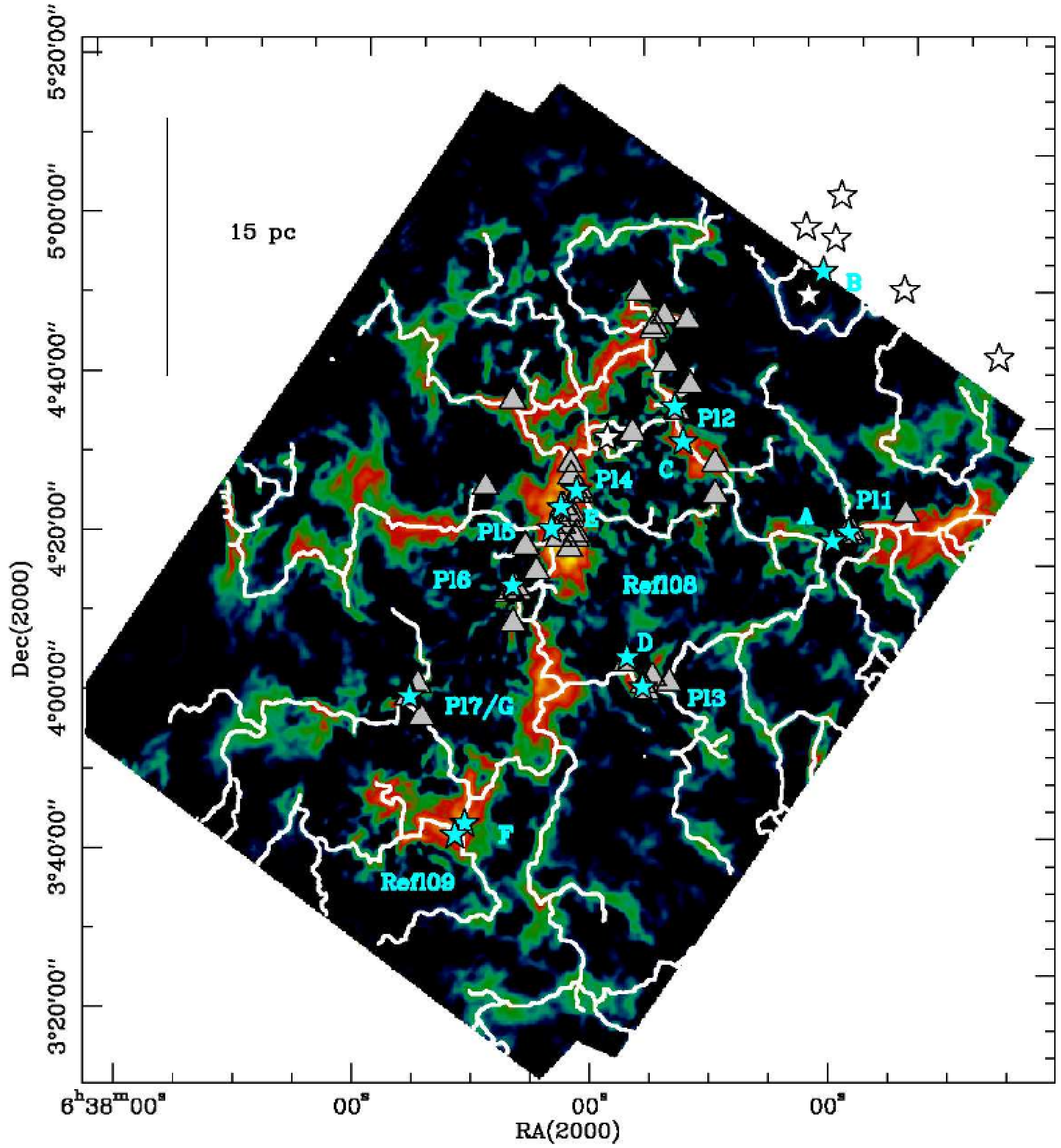

Figure 1.4: Color column density map of the Rosette molecular cloud obtained from Herschel data. The filamentary structure traced by white lines is apparent. Blue stars represent known star-clusters which are located on the junctions of filaments. Figure from Schneider et al. (2012)

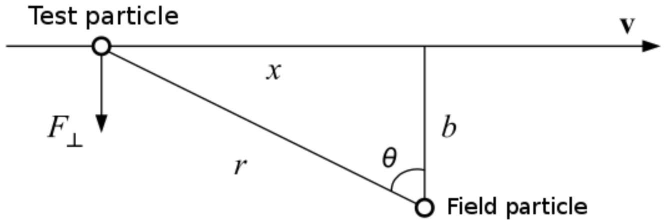

Figure 1.5: Schematic representation of one of the many two-body encounters to which the test particle is subjected. The particles experience a change in velocity due to gravitational forces.

collection of point masses. To distinguish between these two kinds of systems we use the relaxation timescale t_{rl}, defined in equation 1.6. In particular, we say that a system is collisional/collisionless if its lifetime is lesser/greater than t_{rl}. The process which relaxes these system is called two-body relaxation, which is the main process that drives the dynamical evolution of SCs.

1.3.1 Two-Body Relaxation

Two-body relaxation is the result of many long range two-body gravitational interactions. On timescales longer than t_{rl} these interactions slowly redistribute energy between particles and make them lose memory of their initial velocity. The two-body relaxation timescale can be derived following the motion of an individual particle across the SC, and seeking an estimate of the difference between the initial velocity of this particle and the velocity that it has after one system crossing. We consider an idealized system of N particles with mass m, size R and uniform density. The test star passes close to a field star with relative velocity v and impact parameter b as schematized in figure 1.5. Each time this happens, its velocity changes by a small amount, so we assume that $\frac{\delta \mathbf{v}}{\mathbf{v}} << 1$ and that the field star is stationary. $\delta \mathbf{v}$ is perpendicular to $\mathbf{v}$, since the accelerations parallel to $\mathbf{v}$ average to zero. After many of these interactions, the velocity changes completely, or in other words the variation of velocity becomes of the same order of magnitude as the initial velocity:

$$\frac{\Delta \mathbf{v}}{\mathbf{v}} \sim 1. \tag{1.9}$$

The perpendicular gravitational force between the two particles is:

$$F_\perp = \frac{Gm^2}{r^2}\cos\theta = \frac{Gm^2 b}{(b^2+x^2)^{3/2}} = \frac{Gm^2}{b^2}\left[1+\left(\frac{vt}{b}\right)^2\right]^{-3/2}. \tag{1.10}$$

The quantities are defined in figure 1.5. We can infer the change in velocity by integrating the second Newton's law:

$$\delta v = \frac{1}{m}\int_{-\infty}^{+\infty} F_\perp dt = \frac{Gm}{b^2}\int_{-\infty}^{+\infty}\frac{dt}{(1+(vt/b)^2)^{3/2}} = \frac{2Gm}{bv}. \tag{1.11}$$

The surface density of stars in our system is $N/\pi r^2$, so after crossing the system once the subject star suffers

$$\delta n = \frac{N}{\pi R^2} 2\pi b \mathrm{d}b \tag{1.12}$$

encounters with impact parameter between b and $b + \mathrm{d}b$. The resulting mean velocity change is zero because each encounter produces a randomly oriented perturbation, but the quadratic mean velocity change is not:

$$\sum \delta v^2 = \delta v^2 \delta n = 8N \left(\frac{Gm}{vR}\right)^2 \frac{\mathrm{d}b}{b}. \tag{1.13}$$

Integrating this quantity over all the possible impact parameters[2] we obtain:

$$\Delta v^2 = 8N \left(\frac{Gm}{vR}\right)^2 \ln \Lambda \tag{1.14}$$

where $\ln \Lambda$ is called Coulomb logarithm:

$$\ln \Lambda = \frac{b_{\mathrm{min}}}{b_{\mathrm{max}}} = \ln \left(\frac{2\,Gm}{v^2 R}\right) \tag{1.15}$$

and its value for typical SCs is ~ 10. If we assume that the system is in virial equiibrium, the typical velocity of a particle can be expressed as:

$$v^2 = \frac{GNm}{R}. \tag{1.16}$$

Combining equations 1.14, 1.15, 1.16 and eliminating R, we get the change in velocity after one system crossing:

$$\frac{\Delta v^2}{v^2} = \frac{8 \ln N}{N}. \tag{1.17}$$

Requiring the condition of equation 1.9 we get the needed number of crossings to relax the system:

$$n_{\mathrm{cross}} = \frac{N}{8 \ln N}. \tag{1.18}$$

The needed number of crossings is also $n_{\mathrm{cross}} = t_{\mathrm{rl}}/t_{\mathrm{cross}}$, so we can finally derive the two-body relaxation timescale:

$$t_{\mathrm{rl}} = \frac{N}{8 \ln N} \frac{R}{v}. \tag{1.19}$$

After one relaxation timescale, the orbit of the particles is considerably different from the one they would have if the mass was smoothly distributed.

A better formulation with less approximations and based on local parameters rather than global ones was derived by Spitzer (1987):

$$t_{\mathrm{rl}} = \frac{\langle v^2 \rangle^{3/2}}{15.4\, G^2 m \rho \ln \Lambda}, \tag{1.20}$$

where $\langle v^2 \rangle$ is the local velocity dispersion, m is the local mean mass and ρ is the local density.

When applied to SCs, the local relaxation time is usually evaluated at the core (core

---

[2] i.e. between b_{min} and b_{max}, where the former is the minimum distance at which our approximation of small velocity changes holds ($b_{\mathrm{min}} = 2Gm/v^2$), and the latter is the size R of the system.

relaxation timescale t_{rc}) and at the half-mass radius (half-mass radius relaxation timescale t_{rh}). An expression of t_{rh} with handy units is:

$$t_{\mathrm{rh}} = 190\,\mathrm{Myr}\left(\frac{r_{\mathrm{vir}}}{1\,\mathrm{pc}}\right)^{1/2}\left(\frac{M}{10^6\,\mathrm{M}_\odot}\right)^{1/2}\left(\frac{\langle m\rangle}{1\,\mathrm{M}_\odot}\right)^{-1}\left(\frac{\ln\Lambda}{10}\right)^{-1}. \tag{1.21}$$

We can see that t_{rl} is proportional to the size of the system so that YMCs, which are usually compact ($r_{\mathrm{vir}} \lesssim 1\,\mathrm{pc}$), have short relaxation timescales and a faster dynamical evolution. We can evince this also from figure 1.6.

1.3.2 Core Collapse

There are phenomena which happen even faster than two-body relaxation in SCs. One of these is the core collapse or gravothermal catastrophe, which for a realistic YMC happens on a time scale of (Portegies Zwart et al. (2010)):

$$t_{\mathrm{cc}} \sim 0.2\,t_{rl}. \tag{1.22}$$

If a SC survives infant mortality, two-body relaxation makes the core contract. The contraction of the core is a runaway process which leads to a collapse. The physical process behind this is the gravothermal instability which I describe below.
We assume that the SC is in virial equilibrium, hence:

$$2K + W = 0 \tag{1.23}$$

where $W < 0$ is the gravitational potential energy of the cluster. Two-body relaxation redistributes energy between the stars in the core and some of them gain enough kinetic energy to escape from the core to the halo. By escaping, they take away from the core both their potential and kinetic energy. Since the escaping stars are the fastest they take away more kinetic energy than potential energy. The most energetic stars escape the SC, thus the lost kinetic energy cannot be restored by stars flowing from the halo to the core. The core of the cluster becomes sub-virial ($2K + W < 0$) and contracts, increasing the velocity dispersion of its stars and thus the escapers, becoming even more sub-virial. This leads to a catastrophic collapse.
This process occurs even if all the stars have equal mass. If we consider a multi-mass system the collapse is even faster; dynamical friction makes massive stars lose energy and fall towards the center of the cluster, while light stars gain energy and escape. This produces mass segregation with a timescale $t_{df} \propto \frac{\langle m\rangle}{M} t_{rh}$, where $\langle m\rangle$ is the average stellar mass and M is the mass of a massive star undergoing dynamical friction. Dynamical friction is the loss of orbital energy of a body through gravitational interactions with surrounding bodies. An intuition for this effect can be obtained by thinking that as a large object moves through a sea of smaller objects, the gravitational effect of the larger object pulls the smaller objects towards it. This produces a concentration of smaller objects behind the larger body, as it has already moved past its previous position. This concentration of small objects behind the larger body exerts a collective gravitational

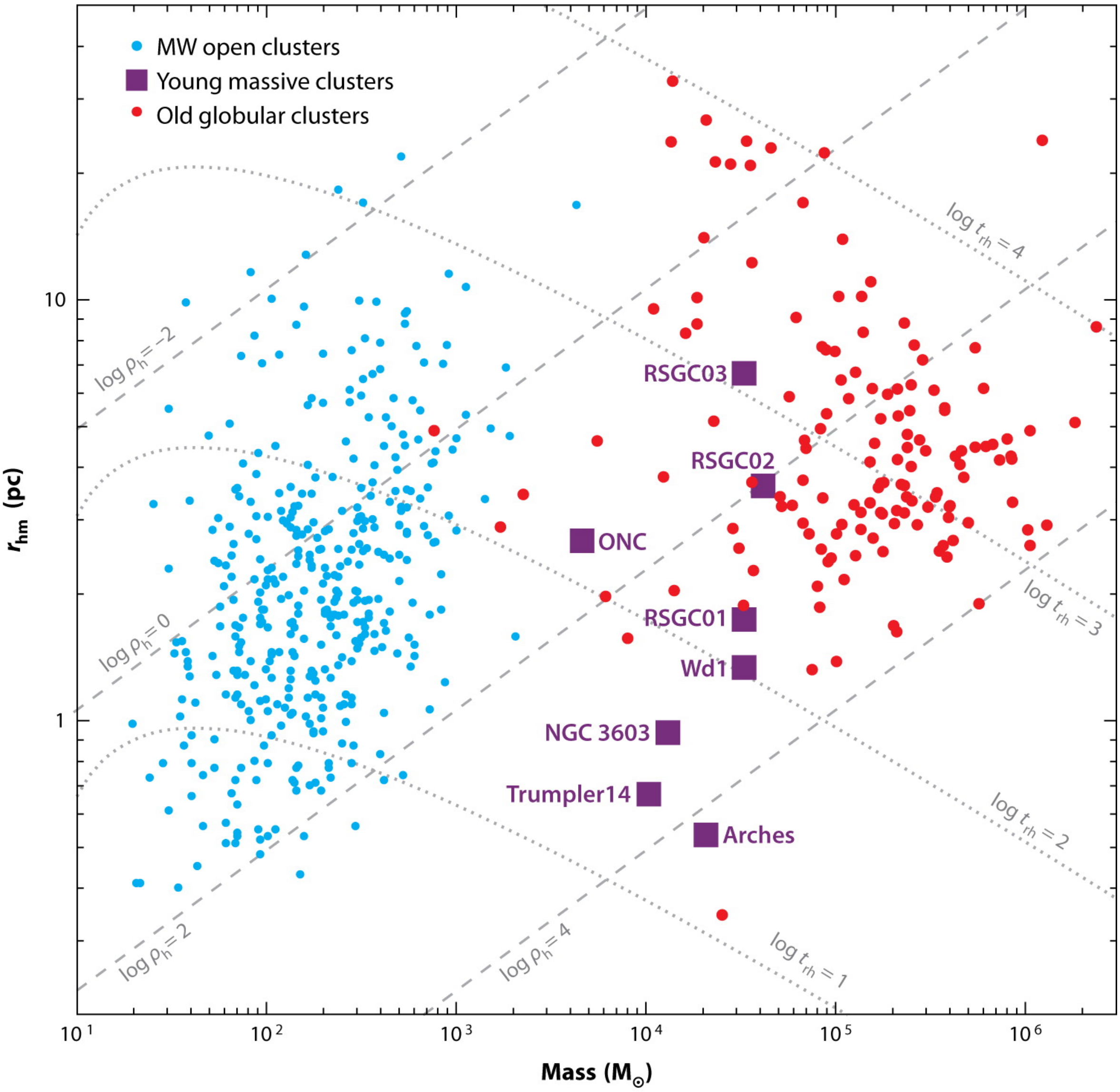

Figure 1.6: Radius-mass diagram of Milky Way SCs. The dotted lines represent constant relaxation timescale. It is clear that YMCs have short relaxation timescale. (figure from Portegies Zwart et al. (2010))

force on the large object, slowing it down.

The collapse should proceed indefinitely, but since we do observe SCs older than the collapse timescale, there should be something that reverts the collapse. In particular, there has to be something that injects energy inside the core and helps it to expand. The energy we are seeking for is stored in binary stars and mass loss by stellar winds and SNe explosion.
During a three-body encounter between a binary and a single star, there is an exchange between the internal energy of the binary and the kinetic energy of the stars. If the binary becomes less bound, the single star transfers part of its kinetic energy to soften the binary. If the binary becomes more bound, the kinetic energy of the system increases and the binary hardens.
The majority of the energy needed to reverse the core collapse is usually provided by the hardening of binaries in the core. Since the core contracts during core collapse, the core density increases and three-body encounters become more frequent, helping the reversal. After the core collapse is reverted the core starts to expand and the half-mass radius of the cluster evolves through the relation (Elson et al. (1987)):

$$r_{hm} \propto t^{2/3} \tag{1.24}$$

1.3.3 Rotation of SCs

Rotation has been observed in different types of SCs. We know that many GCs rotate (Pryor et al. (1986), van Leeuwen et al. (2000), Anderson & King (2003), Pancino et al. (2007), Anderson & van der Marel (2010), Bellazzini et al. (2012), Bianchini et al. (2013), Fabricius et al. (2014) Kimmig et al. (2015), Lardo et al. (2015), Lee (2015)), and signatures of rotation have been found also in YMCs (Hénault-Brunet et al. (2012)) and intermediate age clusters (Davies et al. (2011), Mackey et al. (2013)). Some molecular clouds show velocity gradients that may be connected with rotation, and Li et al. (2017) claim that the molecular cloud G052.24+00.74 rotates.
Some works tried to explain the origin of this feature: Vesperini et al. (2014) claim that rotation in GCs might arise because of violent relaxation in the tidal field of the host galaxy, while Gavagnin et al. (2016) and Mapelli (2017) show that it may be the result of the merger between many sub-clusters and it may be the consequence of the hierarchical assembly scenario. The origin of rotation is still unclear and the fact that we observe rotating SCs with age $t >> t_{rl}$ is surprising, since two-body relaxation should completely erase this feature. Rotation of SCs and its evolution are subject of study of this thesis and will be discussed in chapter 4.

Chapter 2

Aims

Stellar clusters have been long recognized as important environments for astrophysical research and their study has played an important role in understanding the Universe. There are several reasons for which I think studying SCs is interesting.
They contain stars belonging to a wide mass spectrum within a small volume of space. In such dense environments interactions and collisions between stars are frequent, making SCs great laboratories to study dynamics.
Furthermore, we know that the vast majority of stars form in clustered environments. For example, if we take into account O-type stars in the Milky Way, we know that only $\sim 4\%$ of them has not formed in clusters (Portegies Zwart et al. (2010)). Thus, we can say that SCs are the "cradles" of stars and the building blocks of galaxy disks.
Since SCs are made of stars which form more or less simultaneously from the same progenitor molecular cloud, we can also use them to calibrate stellar evolution models and to study the stellar Initial Mass Function (IMF).

In this thesis I investigate the dynamics and kinematics of embedded star clusters during their formation, focusing on their rotation.
I study how SCs form from their progenitor molecular cloud, trying to put some constrains on their formation scenario. Then, since few studies have been published to know why SCs rotate, I try to understand how rotation arises and the dynamical evolution of this feature starting from the work of Mapelli (2017).
Since I perform my N-body simulations starting from the outputs of hydrodynamical simulations of SC's formation, this work may also be useful to solve the problems related to initial conditions for N-body simulations of SCs, which are currently highly idealized.
Finally, I try to compare my results with current observations to check if the rotation observed in young and old clusters is connected to the one which arises in my simulations.

Chapter 3

Numerical Simulations

To reach the aims of this thesis I used numerical simulations, and in particular I used both hydrodynamical and direct N-body codes. Normally these two kinds of codes are not used together, but I needed the features of both for my purposes.
I required hydrodynamical codes to simulate the gas of the parent molecular clouds, their collapse and fragmentation, star formation and the development of the main cluster structures. Then, since hydrodinamical codes have low accuracy on gravitational forces and my thesis focuses on the dynamics and kinematics of SCs, I needed direct N-body codes to have a higher accuracy on the interactions between stars, to better simulate two-body relaxation and the evolution of rotation.

In the following sections I describe the hardware and the charateristics of the codes I used.

3.1 Hydrodynamical Simulations

Star formation takes place in MCs. The mean free paths of particles in MCs tend to be small compared with the sizes of the structures which they belong to, thus it is reasonable to approximate MCs as gas fluids. To model the behaviour of a fluid on a computer it is necessary to take into account gravity and other physical quantities related to fluids, such as pressure and viscosities. In a system of N particles, gravity is governed by Newton's second law:

$$\ddot{\mathbf{r}}_i = -G \sum_{j \neq i} m_j \frac{\mathbf{r_i} - \mathbf{r_j}}{|\mathbf{r_i} - \mathbf{r_j}|^3}, \tag{3.1}$$

where G is the gravitational constant, $\ddot{\mathbf{r}}_i$ is the acceleration, m is the mass and $\mathbf{r}$ is the radius vector. Fluid dynamics is represented by Euler's equations:

$$\frac{\partial \rho}{\partial t} + \nabla \cdot (\rho u) = 0, \tag{3.2}$$

$$\frac{\partial \rho u}{\partial t} + \nabla \cdot (\rho u \times u) + \nabla p = -\rho \nabla \phi, \tag{3.3}$$

$$\frac{\partial \rho e}{\partial t} + \nabla \cdot [\rho u (e + p/\rho)] = -\rho u \cdot \nabla \phi, \tag{3.4}$$

where ρ is mass density, e is the specific energy (i.e. the energy per gas particle), u is the fluid velocity, p is the thermal pressure and ϕ is the gravitational potential of gas.

Since the number of particles is usually very large in hydrodynamical simulations, gravity is solved using indirect methods to speed up the computation. An indirect method is a method which does not calculate the gravitational interaction between all the couples of particles in a system. Instead, it uses a multipole expansion of gravitational force for distant particles, so that less calculations are required.
There are two main types of hydrodynamical codes which discretise fluids in different methods:

- **Eulerian codes**, which break fluids up into a grid of volume elements fixed in space, and evolve the simulation by computing the variations of physical parameters in each volume element, moving mass to or from adjoining neighbours. A popular Eulerian method is called Adaptive Mesh Refinement (AMR), which can increase the resolution of the grid in critical areas where more precision is needed.

- **Lagrangian codes**, which discretise fluids into mass elements with a total mass equal to that of the whole fluid. The fluid is evolved by calculating the forces on each particle and moving them. The most used Lagrangian method is called Smoothed Particle Hydrodynamics (SPH), which represents fluids as particles whose properties are smoothed over a spherical volume.

Eulerian codes are mostly used in situations where shocks are important, while the Lagrangian approach is better suited for dynamics. Since my thesis is focused on dynamics, I chose the SPH code Gasoline (Wadsley et al. (2004)) to perform my hydrodynamical simulations; its properties are described below.

3.1.1 SPH

The SPH method works by dividing the fluid into a set of discrete elements, referred to as particles. These particles have a spatial distance known as the smoothing length h over which their properties are "smoothed" by a kernel function. The smoothing length is defined as the distance at which a particle has a fixed number N of neighbors. The physical quantities of any particle can be obtained by summing the relevant properties of all the particles which lie within the range of the kernel. The contributions of each particle to a property are weighted by the kernel function W. A general smoothed estimate for some quantity f of particle i, given N particles j at positions $\mathbf{r}_j$, takes the form:

$$f_{\text{i,smoothed}} = \sum_{j=1}^{N} f_j W_{ij}(\mathbf{r}_i - \mathbf{r}_j, h_i, h_j), \tag{3.5}$$

where W_{ij} is the kernel function and h_J is a smoothing length indicative of the range of interaction of particle j. For energy and momentum conservation, a symmetric $W_{ij} = W_{ji}$ is required. Gasoline uses the kernel average suggested by Hernquist & Katz (1989):

$$W_{ij} = \frac{1}{2} w(|\mathbf{r}_i - \mathbf{r}_j| / h_i) + \frac{1}{2} w(|\mathbf{r}_i - \mathbf{r}_j| / h_j), \tag{3.6}$$

where $w(r/h)$ is a cubic spline:

$$w(q) = \frac{1}{\pi h^3} \begin{cases} 1 - \frac{3}{2}q^2 + \frac{3}{4}q^3 & 0 \leq q \leq 1; \\ \frac{1}{4}(2-q)^3 & 1 \leq q \leq 2; \\ 0 & q \geq 2 \end{cases} \tag{3.7}$$

with $q = r/h$.
Density ρ_i is calculated from a sum over particle masses m_j:

$$\rho_I = \sum_{j=1}^{N} m_j W_{ij}. \tag{3.8}$$

The momentum equation is expressed as:

$$\frac{d\mathbf{v}_i}{dt} = -\sum_{j=1}^{N} m_j \left(\frac{P_i}{\rho_i^2} + \frac{P_j}{\rho_j^2} + \Pi_{ij} \right) \nabla_i W_{ij}, \tag{3.9}$$

where P is pressure, $\mathbf{v}$ is velocity and Π is the artificial viscosity term, given by:

$$\Pi_{ij} = \begin{cases} \frac{-\alpha\frac{1}{2}(c_i+c_j)\mu_{ij}+\beta\mu_{ij}^2}{\frac{1}{2}(\rho_i+\rho_j)} & \text{if } \mathbf{v}_{ij}\cdot\mathbf{r}_{ij} < 0 \\ 0 & \text{if } \mathbf{v}_{ij}\cdot\mathbf{r}_{ij} < 0 \end{cases}, \tag{3.10}$$

where $\mu_{ij} = \frac{h(\mathbf{v}_{ij}\cdot\mathbf{r}_{ij})}{\mathbf{r}_{ij}^2+0.01(h_i+h_j)^2}$, $\mathbf{r}_{ij} = \mathbf{r}_i - \mathbf{r}_j$, $\mathbf{v}_{ij} = \mathbf{v}_i - \mathbf{v}_j$, and c is the sound speed. $\alpha = 1$ and $\beta = 2$ are coefficients used to represent shear and Von Neumann-Richtmyer viscosities respectively.

Gasoline includes recipes to treat gas cooling. There are three main options:

- Adiabatic: gas does not exchange heat with the environment.
- Isothermal: gas temperature is constant.
- Cooling: gas temperature changes according to a cooling function (Sutherland & Dopita (1993)).

If the cooling option is active, a function is added to gas equations that accounts for cooling or heating processes:

$$\frac{de}{dt} = -\frac{P}{\rho}\nabla\cdot\mathbf{v} - \frac{\Lambda(e,\rho)}{\rho}, \tag{3.11}$$

where e is the specific thermal energy, P is gas pressure, ρ is gas density, v is gas velocity and Λ is the cooling function. The cooling functions of Sutherland & Dopita (1993) are suited for metal cooling.
MCs have temperatures and densities that make them cool through dust rather than metals, so in my simulations I have used a different cooling algorithm, which is the same as that described in Boley (2009) and Boley et al. (2010). According to this algorithm, the divergence of the flux is $\nabla \cdot F = -(36\pi)^{1/3}\, s^{-1}\sigma(T^4 - T_{\mathrm{irr}}^4)(\Delta\tau + 1/\Delta\tau)^{-1}$, where σ is the Stephan's constant, T_{irr} is the incident irradiation, $s = (m/\rho)^{1/3}$ and $\Delta\tau = s\kappa\rho$,

for the local opacity κ, particle mass m and density ρ.
I used D'Alessio et al. (2001) Planck and Rosseland opacities, with a $1\,\mu$m maximum grain size. Such opacities are obtained from models of irradiated T Tauri disks and are appropriate for temperatures in the range of a few Kelvins up to thousands of Kelvins. In my simulations $T_{\rm irr} = 10\,$K everywhere.

3.1.2 Gravity

Gasoline is built on the Pkdgrav framework (Stadel (2001)) and thus uses the same gravity algorithms. Pkdgrav is a tree-code: a kind of code that solves gravity with an indirect method. It is mostly based on the Barnes-Hut algorithm (Barnes & Hut (1986)). The name *"tree-code"* comes from the fact that the simulation box is divided into sub-boxes, sub-sub-boxes and so on. The big box is the root of the tree, the sub-boxes are the branches and the smallest sub-boxes are the leaves. The Barnes-Hut algorithm continues to divide until each cell has a single or no particle inside of it (Figure 3.1), while in Pkdgrav the depth of the tree is chosen so that there are at most 8 particles in the leaf boxes (buckets).
After creating the tree, the code can compute the gravitational force exerted on each particle. If a group of particles is sufficiently far, the code estimates the cumulative force of the group rather than calculating the force exerted by every single particle. In Barnes-Hut algorithm, the group is replaced by a single particle with the position at the center of mass, and the total mass of the group as the mass. Gasoline uses a hexadecapole multipole expansion of the gravitational potential, which is more accurate but computationally heavier.

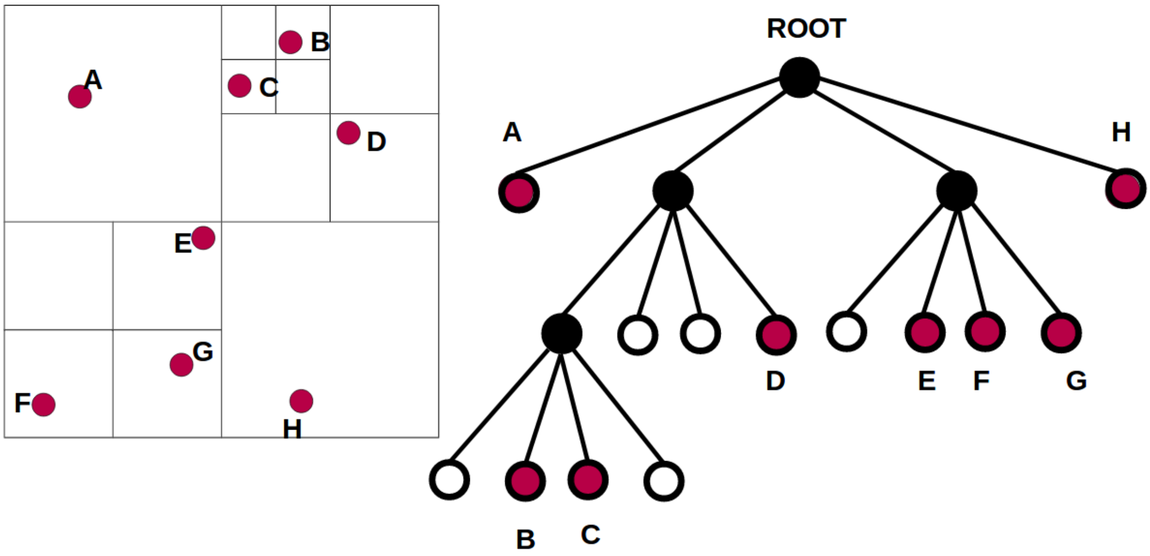

Figure 3.1: Diagram of a Barnes-Hut tree, showing the division into cells (left) and the tree structure (right).

To determine if a particle is sufficiently far to avoid direct calculation, the code assigns

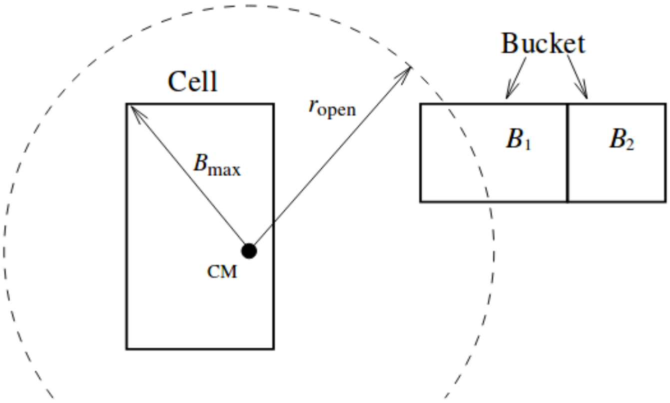

Figure 3.2: Opening radius for a cell in the tree, intersecting bucket B_1 but not B_2. This cell is “opened” while walking the tree for B_1, while it is considered too far and avoids direct calculation for B_2.

to each cell of the tree an opening radius about its center of mass. This is defined as:

$$r_{\text{open}} = \frac{2B_{\text{max}}}{\sqrt{3}\theta} \tag{3.12}$$

where B_{max} is the maximum distance from a particle in the cell to the center of mass of the cell. The opening angle θ is a user defined accuracy parameter.
The opening radii are used as follows: for each bucket B_i, Gasoline starts descending the tree, opening those cells whose r_{open} intersect with B_i (Figure 3.2). If a cell is opened, then Gasoline repeats the intersection test with B_i for the cell’s children. Otherwise, the cell is considered sufficiently far to avoid direct calculation. When Gasoline reaches the leaves of the tree and a bucket B_j is opened, all of B_j’s particles are subject to direct calculation. Once the tree has been traversed in this manner, the code can calculate the gravitational acceleration for each particle of B_i.

Sometimes particles can approach too much so that the gravitational force (eq. 3.1) between them can diverge and become unphysical. This happens only if the particles are treated as point objects with no spatial extension. To overcome this problem, numerical simulations exploit a technique called softening. Gasoline implements softening by smoothing the mass of the particles in space using the same spline kernels employed in the SPH calculation. The distance over which the mass is smoothed is called gravitational softening ϵ, and it may vary for each particle. This means that the gravitational forces between two particles i and j vanish at zero separation and return to Newtonian $1/r^2$ at a separation of $\epsilon_i + \epsilon_j$. The value of ϵ can be taken as the average distance betwen particles, or can be estimated using the virial radius of the system and the total number of particles in the simulation N:

$$\epsilon = \left(\frac{4\pi R_{\text{vir}}^3}{3} \right)^{1/3} N^{-1/3}. \tag{3.13}$$

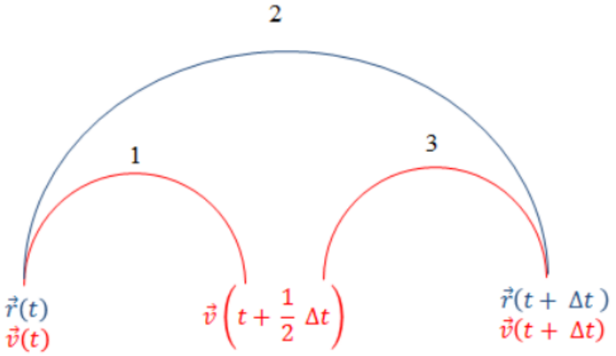

Figure 3.3: Scheme of a leapfrog method using KDK. The kicks are represented by red lines, the drift by the blue line.

3.1.3 Integration

To integrate the evolution of the systems, Gasoline incorporates the leapfrog scheme described as Kick-Drift-Kick (KDK) in Quinn et al. (1997). Here is a brief simplified description of the algorithm for a particle with position **r** and velocity **v**, going from time t to time $t + \Delta t$ (figure 3.3):

1. Kick: the velocity **v** is kicked to an intermediate timestep.

$$\mathbf{v}(t+\frac{1}{2}\Delta t) = \mathbf{v}(t) + \frac{1}{2}\Delta t\mathbf{a}(t). \tag{3.14}$$

2. Drift: the position **r** is drifted.

$$\mathbf{r}(t+\Delta t) = \mathbf{r}(t) + \mathbf{v}(t+\frac{1}{2}\Delta t)\Delta t. \tag{3.15}$$

3. Kick: the velocity is kicked again to its final value.

$$\mathbf{v}(t+\Delta t) = \mathbf{v}(t+\frac{1}{2}\Delta t) + \frac{1}{2}\Delta t\mathbf{a}(t+\Delta t). \tag{3.16}$$

The final values of position and velocity are:

$$\mathbf{r}(t+\Delta t) = \mathbf{r}(t) + \mathbf{v}(t)\Delta t + \frac{1}{2}(\Delta t)^2\mathbf{a}(t); \tag{3.17}$$

$$\mathbf{v}(t+\Delta t) = \mathbf{v}(t) + \frac{1}{2}\Delta t\mathbf{a}(t) + \frac{1}{2}\Delta t\mathbf{a}(t+\Delta t). \tag{3.18}$$

The real algorithm used by Gasoline is more complex since it also includes thermal energy. The leapfrog scheme requires only one force evaluation and minimum storage.

3.1.4 Star Formation

Simulating the hydrodynamical formation of every single star of a SC would be too complex and would require an incredibly long computation time. To overcome this problem, simulations of MCs exploit the technique of **sink particles**. A sink particle represents a star and it is affected only by gravity, not contributing to pressure and other gas-related quantities.
If a clump of gas particles meets some specific criteria, the simulation replaces it with a sink particle. A density threshold is defined and any gas particles exceeding this threshold, along with their neighbours, are considered for sink formation. Several criteria must be met:

1. the ratio α of thermal to gravitational potential energy of the group must be < 0.5.
2. The sum of α and β, the ratio of rotational energy to gravitational potential energy, must be < 1.
3. The total energy of the group must be negative.
4. The divergence of the acceleration must be negative.

If these tests are passed, a sink is created with the total mass and momentum of the seed gas particles (Figure 3.4).
Sinks may even accrete gas particles. Accretion onto the sink is achieved by assigning it an accretion radius and testing particles which pass within it. Particles which are bound to the sink with a specific angular momentum less than that required to form a circular orbit at the accretion radius are accreted.

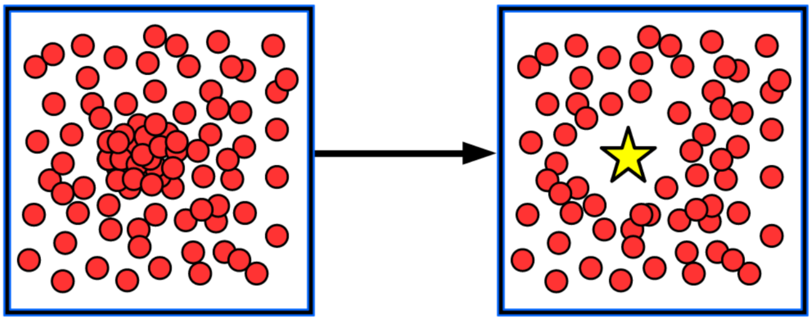

Figure 3.4: Scheme of the creation of a sink particle. If all the criteria are met, the clump of gas particles is converted to a sink particle with the total mass and momentum of the clump.

3.1.5 Hardware

To perform my SPH simulations I used the Galileo cluster at the italian supercomputing centre CINECA (http://www.hpc.cineca.it/hardware/galileo). Galileo has 8256 cores, with a maximum number of 16 cores per node, and has a RAM of 128GB per

node.
Hydrodynamical simulations are usually run on Central Processing Units (CPUs).

3.2 Direct N-Body Simulations

As described in section 1.3, the phase subsequent to gas evaporation in SCs is dominated by purely stellar dynamical processes. This means that at this stage we can neglect the effects of gas and simulate the systems with a direct summation N-body code.
A direct summation N-body code calculates the force of gravity for all the couples of particles in the system. These codes are useful to evolve collisional systems like SCs where the stellar density is so high that single gravitational interactions between particles are frequent, strong and affect the overall evolution. These codes do not include the treatment of gas, but they integrate gravity with much higher acuracy than hydrodynamical codes since they do not use approximations.
In my thesis I use the direct summation N-body algorithm to simulate the dynamical evolution of the SCs which form in hydrodynamical simulations.
The code I chose is HiGPUs (Capuzzo-Dolcetta et al. (2012)), which implements an Hermite's 6th order time integration scheme with block time steps, allowing both high precision and speed.

3.2.1 Block Time Steps

When integrating an N-body system, choosing the same timestep for all particles may be too computationally expensive. Particles which undergo close encounters would need short timesteps, since they're experiencing rapid force variations. On the other hand, other particles subject to weaker interactions can be integrated with longer timesteps without losing much accuracy. Thus, it is convenient to choose different timesteps for particles depending on how fast the forces acting on them are changing.
HiGPUs evaluates the timesteps using the generalised Aarseth criterion (Nitadori & Makino (2008)). For a particle i with acceleration $\mathbf{a}_i$ the timestep is:

$$\Delta t_i = \eta \left(\frac{A_i^{(1)}}{A_i^{(4)}} \right)^{1/3}, \tag{3.19}$$

where:

$$A_i^{(k)} = \sqrt{|\mathbf{a}_i^{(k-1)}||\mathbf{a}_i^{k+1}| + |\mathbf{a}_i^{(k)}|^2}. \tag{3.20}$$

η is a user defined quantity called accuracy parameter and $\mathbf{a}_i^{(k)}$ is the k-th time derivative of acceleration.
Having a different timestep for each particle, however, is computationally expensive and may create problems with synchronization and parallelization of the code. To solve this problem, HiGPUs uses the technique of block timesteps: particles are grouped replacing their individual timesteps Δt_i with a block timestep:

$$\Delta t_{i,b} = \left(\frac{1}{2} \right)^n, \tag{3.21}$$

where n is chosen according to:

$$\left(\frac{1}{2}\right)^n \leq \Delta t_i \leq \left(\frac{1}{2}\right)^{n-1} \tag{3.22}$$

.

This choice imposes that $t/\Delta t_{i,b} \in \mathbb{N}$, which is good for synchronizing the particles. To avoid bottlenecks, a minimum treshold for $\Delta t_{i,b}$ is usually set to $\Delta t_{\min} = 2^{-23}$.

3.2.2 Integration

We consider a system of N stars and we assume that the i-th particle has, at time $t_{c,0}$, a position $\mathbf{r}_{i,0}$, a velocity $\mathbf{v}_{i,0}$, an acceleration $\mathbf{a}_{i,0}$, a jerk $\dot{\mathbf{a}}_{i,0}$, a snap $\ddot{\mathbf{a}}_{i,0}$, a crackle $\dddot{\mathbf{a}}_{i,0}$ and an individual timestep $\Delta t_{i,0}$.
Calling m the number of particles belonging to the same time-block, which have to be evolved to the same time $t_{c,0} + \Delta t_{i,0}$, the generic Hermite's step is composed by three substeps: a prediction, an evaluation and a correction.

1. Prediction step: positions, velocities and accelerations of all stars are predicted using their known values:

$$\mathbf{r}_{i,\text{pred}} = \mathbf{r}_{i,0} + \mathbf{v}_{i,0}\Delta t_{i,0} + \frac{1}{2}\mathbf{a}_{i,0}\Delta t_{i,0}^2 + \frac{1}{6}\dot{\mathbf{a}}_{i,0}\Delta t_{i,0}^3 + \frac{1}{24}\ddot{\mathbf{a}}_{i,0}\Delta t_{i,0}^4 + \frac{1}{120}\dddot{\mathbf{a}}_{i,0}\Delta t_{i,0}^5, \tag{3.23}$$

$$\mathbf{v}_{i,\text{pred}} = \mathbf{v}_{i,0} + \mathbf{a}_{i,0}\Delta t_{i,0} + \frac{1}{2}\dot{\mathbf{a}}_{i,0}\Delta t_{i,0}^2 + \frac{1}{6}\ddot{\mathbf{a}}_{i,0}\Delta t_{i,0}^3 + \frac{1}{24}\dddot{\mathbf{a}}_{i,0}\Delta t_{i,0}^4, \tag{3.24}$$

$$\mathbf{a}_{i,\text{pred}} = \mathbf{a}_{i,0} + \dot{\mathbf{a}}_{i,0}\Delta t_{i,0} + \frac{1}{2}\ddot{\mathbf{a}}_{i,0}\Delta t_{i,0}^2 + \frac{1}{6}\dddot{\mathbf{a}}_{i,0}\Delta t_{i,0}^3. \tag{3.25}$$

2. Evaluation step: the accelerations of $m \leq N$ particles as well as their first and second time derivatives are evaluated using the above predicted data. The mutual interaction between the i-th particle and the remaining $N-1$ is described by the following relations:

$$\mathbf{a}_{i,1} = \sum_{j=1,\, j\neq i}^{N} \mathbf{a}_{ij,1} = \sum_{j=1,\, j\neq i}^{N} m_j \frac{\mathbf{r}_{ij}}{r_{ij}^3}, \tag{3.26}$$

$$\dot{\mathbf{a}}_{i,1} = \sum_{j=1,\, j\neq i}^{N} \dot{\mathbf{a}}_{ij,1} = \sum_{j=1,\, j\neq i}^{N} \left(m_j \frac{\mathbf{v}_{ij}}{r_{ij}^3} - 3\alpha_{ij}\mathbf{a}_{ij,1} \right), \tag{3.27}$$

$$\ddot{\mathbf{a}}_{i,1} = \sum_{j=1,\, j\neq i}^{N} \ddot{\mathbf{a}}_{ij,1} = \sum_{j=1,\, j\neq i}^{N} \left(m_j \frac{\mathbf{a}_{ij}}{r_{ij}^3} - 6\alpha_{ij}\dot{\mathbf{a}}_{ij,1} - 3\beta_{ij}\mathbf{a}_{ij,1} \right), \tag{3.28}$$

where $\mathbf{r}_{ij} = \mathbf{r}_{j,\text{pred}} - \mathbf{r}_{i,\text{pred}}$, $\mathbf{v}_{ij} = \mathbf{v}_{j,\text{pred}} - \mathbf{v}_{i,\text{pred}}$, $\mathbf{a}_{ij} = \mathbf{a}_{j,\text{pred}} - \mathbf{a}_{i,\text{pred}}$, $\alpha_{ij} r_{ij}^2 = \mathbf{r}_{ij} \cdot \mathbf{v}_{ij}$, $\beta_{ij} r_{ij}^2 = v_{ij}^2 + \mathbf{r}_{ij} \cdot \mathbf{a}_{ij} + \alpha_{ij}^2 r_{ij}^2$.

3. Correction step: positions and velocities of the mentioned m particles are updated and corrected using the above evaluated accelerations and their time derivatives:

$$\mathbf{v}_{i,\text{corr}} = \mathbf{v}_{i,0} + \frac{\Delta t_{i,0}}{2}(\mathbf{a}_{i,1} + \mathbf{a}_{i,0}) - \frac{\Delta t_{i,0}^2}{10}(\dot{\mathbf{a}}_{i,1} - \dot{\mathbf{a}}_{i,0}) + \frac{\Delta t_{i,0}^3}{120}(\ddot{\mathbf{a}}_{i,1} + \ddot{\mathbf{a}}_{i,0}), \tag{3.29}$$

$$\mathbf{r}_{i,\text{corr}} = \mathbf{r}_{i,0} + \frac{\Delta t_{i,0}}{2}(\mathbf{v}_{i,\text{corr}} + \mathbf{v}_{i,0}) - \frac{\Delta t_{i,0}^2}{10}(\mathbf{a}_{i,1} - \mathbf{a}_{i,0}) + \frac{\Delta t_{i,0}^3}{120}(\dot{\mathbf{a}}_{i,1} + \dot{\mathbf{a}}_{i,0}). \tag{3.30}$$

HiGPUs implements softening modifying Newton's equation:

$$F_{ij} = -Gm_im_j \frac{\mathbf{r}_i - \mathbf{r}_j}{(|\mathbf{r}_i - \mathbf{r}_j| + \epsilon^2)^{3/2}}. \tag{3.31}$$

ϵ is the smoothing gravitational length, which can be chosen by the user for each particle. This operation corresponds to the replacement of point masses with Plummer spheres of scale length ϵ (Plummer (1911)).

3.2.3 Hardware

Even though the operations needed to integrate a gravitational N-body system are simple, the fact that they should be repeated for each couple of particles makes the integration time scale as $N(N-1)$.
Initially, direct N-body simulations were performed using special computers called GRAPE (http://jun.artcompsci.org/index-e.html), specifically designed for this purpose. Recently, however, Gaburov et al. (2009) developed the SAPPORO library, which emulates GRAPE's features on NVIDIA Graphic Processing Units (GPUs) using the CUDA environment. This is possible because GPUs are made of many small processors capable of working in parallel. This way, insted of having few powerful processors (CPUs), we have many slower ones (GPUs), each of which can perform the many simple operations needed (Figure 3.5).
GPUs and GRAPE have similar performances (Figure 3.6), but GPUs are much cheaper.

Thanks to the implementation of OpenMP, MPI, CUDA and OpenCL, HiGPUs is a really versatile code, capable of running simulations on CPUs and both NVIDIA/AMD GPUs.
I ran all the direct N-body simulation for this thesis on a NVIDIA GeForce Titan Black of the ForDyS research group (http://web.pd.astro.it/mapelli/group.html).

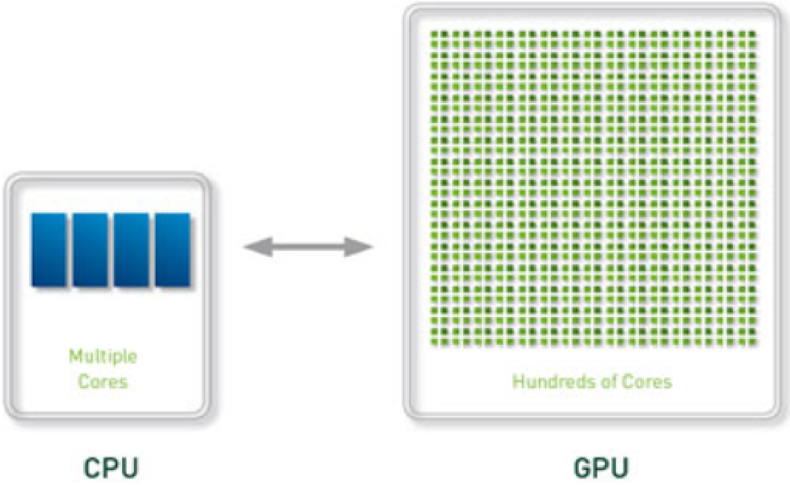

Figure 3.5: Comparison between a CPU and a GPU. GPUs have many ($\sim 10^3$) low-power processors, while CPUs have $1-16$ powerful cores.

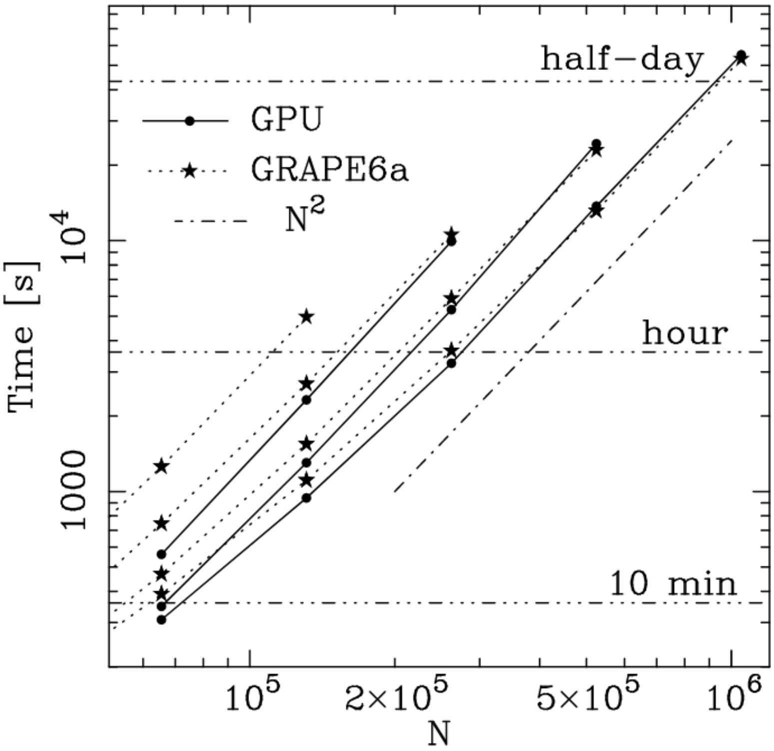

Figure 3.6: Computation time as function of the number of particles using GPUs (solid line with bullets) or GRAPE (dotted line with stars). From top to bottom, one, two, or four GPUs and one, two, four and eight GRAPEs. The dashed-dotted line shows the expected N^2-scaling, offset not to overlap with the measurements. Figure from Gaburov et al. (2009).

Chapter 4

Results

In this chapter I present and discuss the data obtained from the simulations. I mainly used Python and C++ scripts to extrapolate and analyze data.
My results support the idea that rotation is quite common in young massive star clusters and may survive for a long time (longer than a two-body relaxation timescale).

4.1 Initial Conditions

I start from SPH simulations of three turbulence-supported molecular clouds named A, B and C[1] (Mapelli (2017)). The clouds are initially spherical and have homogeneus density. They are marginally self-bound, which means that for each cloud the total kinetic energy is approximately equal to the total gravitational potential:

$$\frac{K}{|U|} = 1. \tag{4.1}$$

Supersonic turbulence in the cloud is generated from a velocity field with an imposed power spectrum $P(k)$, varying as k^{-4}. The velocity field is created by generating a grid of velocities using a divergence free Gaussian field randomly distributed using a Monte Carlo method. This yields a velocity dispersion $\sigma(l)$, varying as $l^{1/2}$, chosen to agree with the Larson's scaling relation (equation 1.8). Clouds A and B are two different realizations of the same cloud, with $M = 4.3 \times 10^4\,\mathrm{M}_\odot$ and $R = 8.8$pc but different random seeds for turbulence. Cloud C has $M = 10^4\,\mathrm{M}_\odot$ and $R = 5.4$pc. Each cloud has approximately the same initial density $\rho \sim 10^{-21}\,\mathrm{g/cm^3}$ and temperature $\mathrm{T} = 10\,K$, and is composed of 10^7 equal-mass gas particles.
The density treshold for sink particles creation is set to $\rho_{th} = 10^{-17}\,\mathrm{g/cm^3}$. The sink accretion radius is $r_{\mathrm{acc}} = 2\tilde{\epsilon}$, where $\tilde{\epsilon}$ is the softening length ($\tilde{\epsilon} = 10^{-6} - 10^{-4}\,\mathrm{pc}$, depending on the resolution of the simulation).
The initial conditions of each cloud are summarised in Table 4.1.

---

[1] Cloud D, whose properties are reported in Table 4.1, is currently being simulated and will not be discussed in this thesis.

Table 4.1: Initial conditions of the simulated MCs. The second column gives the total mass, followed by cloud radius, number of equal-mass gas particles and temperature.

Cloud	$M\,[\mathrm{M}_\odot]$	$R\,[\mathrm{pc}]$	N_{gas}	$T\,[\mathrm{K}]$
A	4.3×10^4	8.8	10^7	10
B	4.3×10^4	8.8	10^7	10
C	1.0×10^4	5.4	10^7	10

4.2 SC Formation and Transition to Direct N-body Code

In my simulations, SCs form following the hierarchical clustering scenario. The initial evolution of the molecular cloud is due to the turbulent motions present in the gas. The supersonic turbulence leads to the development of shocks in the gas, producing filamentary structures (Bate et al. (2003)). The most dense regions in the filamentary structures become self-gravitating and collapse to form stars. Star formation begins after 1.3 Myr in clouds A and B, and after 1.5 Myr in cloud C. Stars along filaments and the residual gas are attracted by their mutual gravitational forces and fall towards each other creating local subclusters. The number of stars in each subcluster increases as stars continue to form nearby. After the majority of the gas is depleted by star formation, subclusters sink towards each other to form the final single cluster structure, which in all my runs has a size of approximately 1 pc.
Some snapshots of cloud A which summarise the formation of the SC are reported in figure 4.1.
To verify that this formation scenario is connected with large scale supersonic turbulence, I have performed a test run seeded with small scale turbulence ($P(k) \propto k^4$). As shown in Figure 4.2, this cloud collapses monolitically. This could mean that the large scale turbulence we observe in MCs may support the hierarchical assembly scenario.

For each simulation, at $t = 4\,\mathrm{Myr}$ (i.e. approximately twice the free-fall time scale of the cloud), I remove the gas particles and use the positions, velocities and masses of sink particles as initial conditions for HiGPUs, which will continue to evolve the SC with better accuracy on dynamical interactions.
Gas removal is mainly justified by two facts:

- The gas fraction within 1 pc from the center of mass of the SCs is less than 0.15 (Figure 4.3). The gas fraction $f_{\mathrm{gas}}(r)$ is defined as:

$$f_{\mathrm{gas}}(r) = \frac{m_{\mathrm{gas}}(r)}{m_{\mathrm{gas}}(r) + m_{\mathrm{star}}(r)}, \tag{4.2}$$

  where r is the distance from the center of mass, m_{gas} is the gas mass within r and m_{star} is the stellar mass within r.

- After 4 Myr, the first SN explosions would start to explode, evaporating the remaining gas.

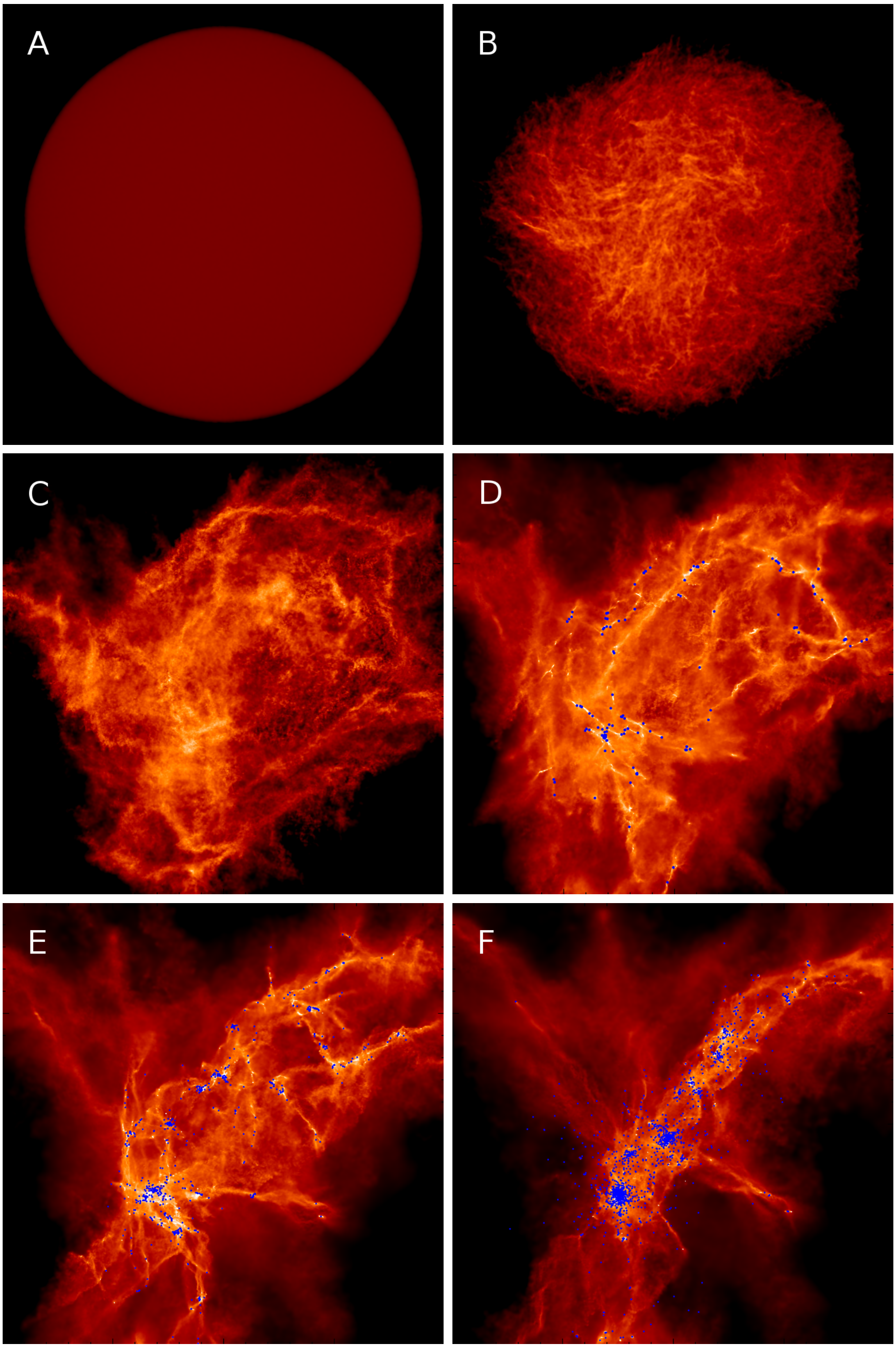

Figure 4.1: Projected density of gas in cloud A at different timesteps. Blue dots represent stars. The boxes measure 20 × 20pc. From left to right and from top to bottom: $t = 0\,\mathrm{Myr}, 0.2\,\mathrm{Myr}, 1\,\mathrm{Myr}, 2\,\mathrm{Myr}, 3\,\mathrm{Myr}, 4\,\mathrm{Myr}$. The cloud is initially uniform and spherical (A), then the filamentary structure begins to develop due to turbulence and self-gravity (B and C). After 2 Myr stars have formed along the filaments (D). The stars fall towards local potential minima and hence form subclusters (E). The subclusters sink towards each other and begin to form the main cluster structure (F).

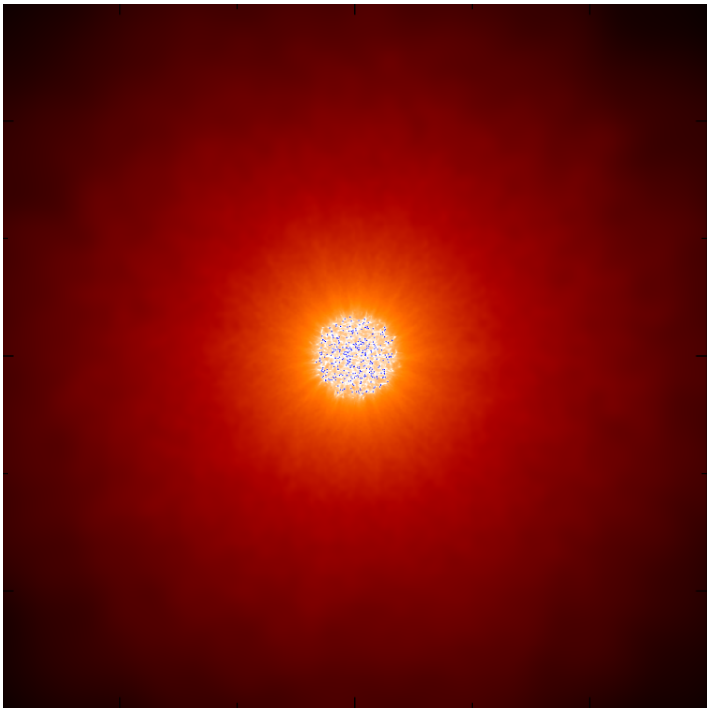

Figure 4.2: Projected density of gas in test run with $P(k) \propto k^4$ at $t = 1.8\,\mathrm{Myr}$. Small blue dots represent stars. The box measures $6 \times 6\mathrm{pc}$. Stars form in a unique compact structure rather than along filaments.

4.3 Mass Profiles

The mass profiles $M(r)$ of the SCs allow us to see how their mass is distributed in space. After 4 Myr, the main cluster of each simulation has fully assembled. All the simulated star clusters develop a similar mass profile, as shown in Figure 4.4. Usually, direct N-body simulations of SCs start from idealized distributions such as Plummer sphere or King models (King (1966)). The mass profile of a Plummer Sphere with total mass M is:

$$M(r) = M\frac{r^3}{(r^2 + a^2)^{3/2}}, \tag{4.3}$$

where a is a scale parameter also known as Plummer radius and r is the distance from the centre. The mass profiles of my SCs are not idealized, since they come from the hydrodynamical simulations. A comparison between a Plummer sphere and the mass profiles of my SCs is shown in figure 4.4.

4.4 Rotation

In my simulations the hierarchical assembly scenario leads to the onset of rotation in SCs. Rotation arises from the torques exerted by gas filaments and clumps while they merge with the main proto-cluster structure with non-zero angular momentum. The SCs inherit the rotation signature from the parent molecular clouds (Mapelli (2017)). To measure rotation, I project the stars onto the xy plane, defined as the plane

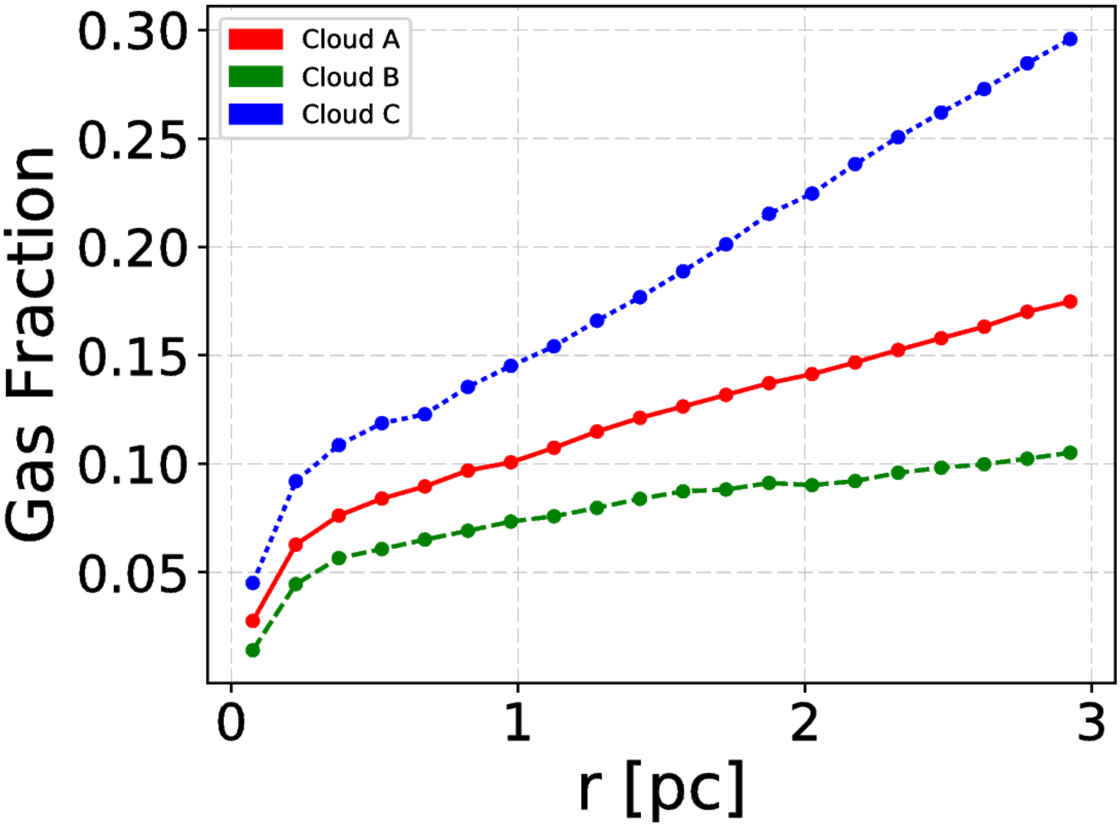

Figure 4.3: Gas fraction at $t = 4\,\mathrm{Myr}$ within $3\,\mathrm{pc}$ from the center of mass of the cloud. Few gas particles remain nearby the SCs.

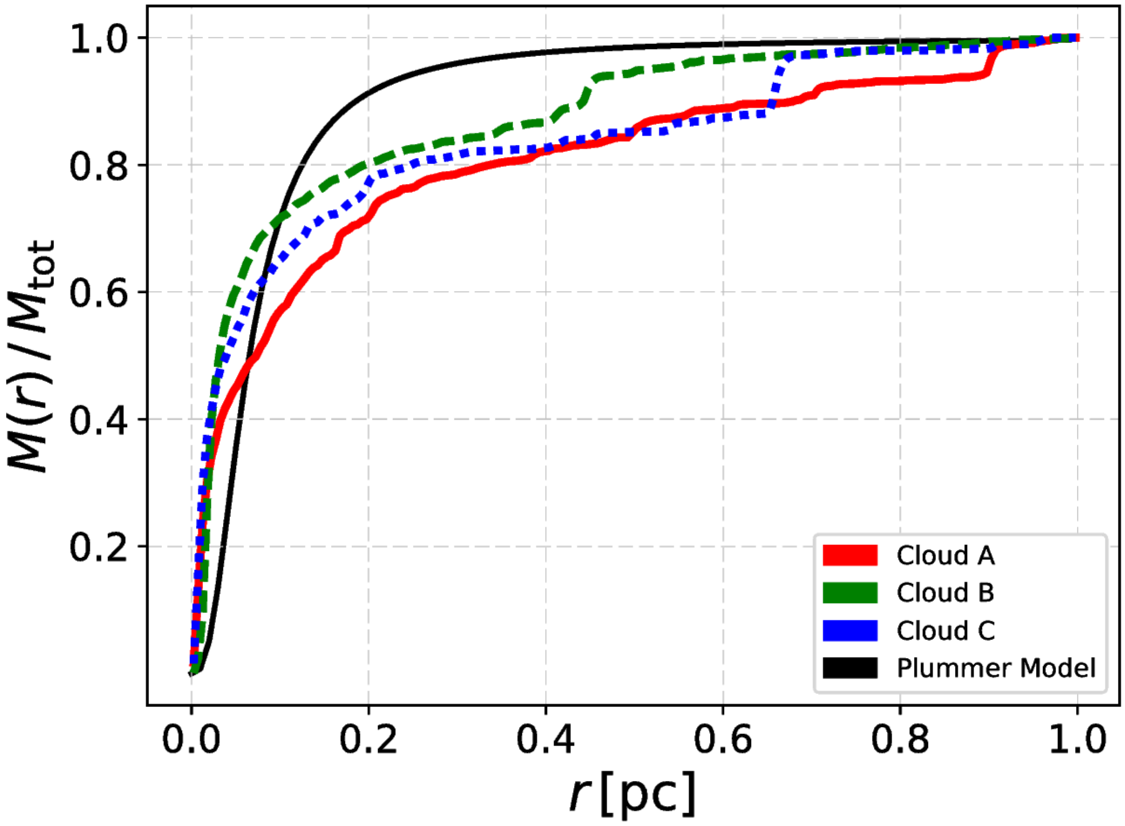

Figure 4.4: Normalized mass profiles of my SCs at $t = 4\,\mathrm{Myr}$. The red, green and blue lines represent run A, B and C respectively. The black line represents a Plummer sphere with scale factor $a = 5 \times 10^{-2}\,\mathrm{pc}$.

perpendicular to the total angular momentum vector (which is thus aligned along the z axis). If the cluster rotates, the stellar projected velocities v_x and v_y show a red-shifted and a blue-shifted component. The presence of this feature along v_z as well would indicate that the cluster is undergoing subvirial collapse (Proszkow et al. (2009)). The main difference between the signature of genuine rotation and that of subvirial collapse is that the latter has no preferential plane (and ideally zero angular momentum vector), while the former is maximum in the plane perpendicular to the angular momentum vector. My simulated SCs are subvirial ($K/|U| \sim 0.25$), so I expect to see this effect. However, as shown by Mapelli (2017), this effect is much weaker than the signature of rotation.
At $t = 6\,\mathrm{Myr}$ the SCs clearly rotate, as shown in Figure 4.5.

One of the main aims of this thesis is to study the evolution of rotation to see how long it lasts in SCs. I expect that several processes would affect and quench rotation. The expulsion of the residual gas, the galactic tidal field, magnetic braking (Galli et al. (2006)) and most importantly the dynamics of stars should remove angular momentum from the cluster, progressively erasing rotation. In particular, two-body relaxation makes stars lose memory of their initial velocity, so I expect that at $t = t_{rh}$ rotation

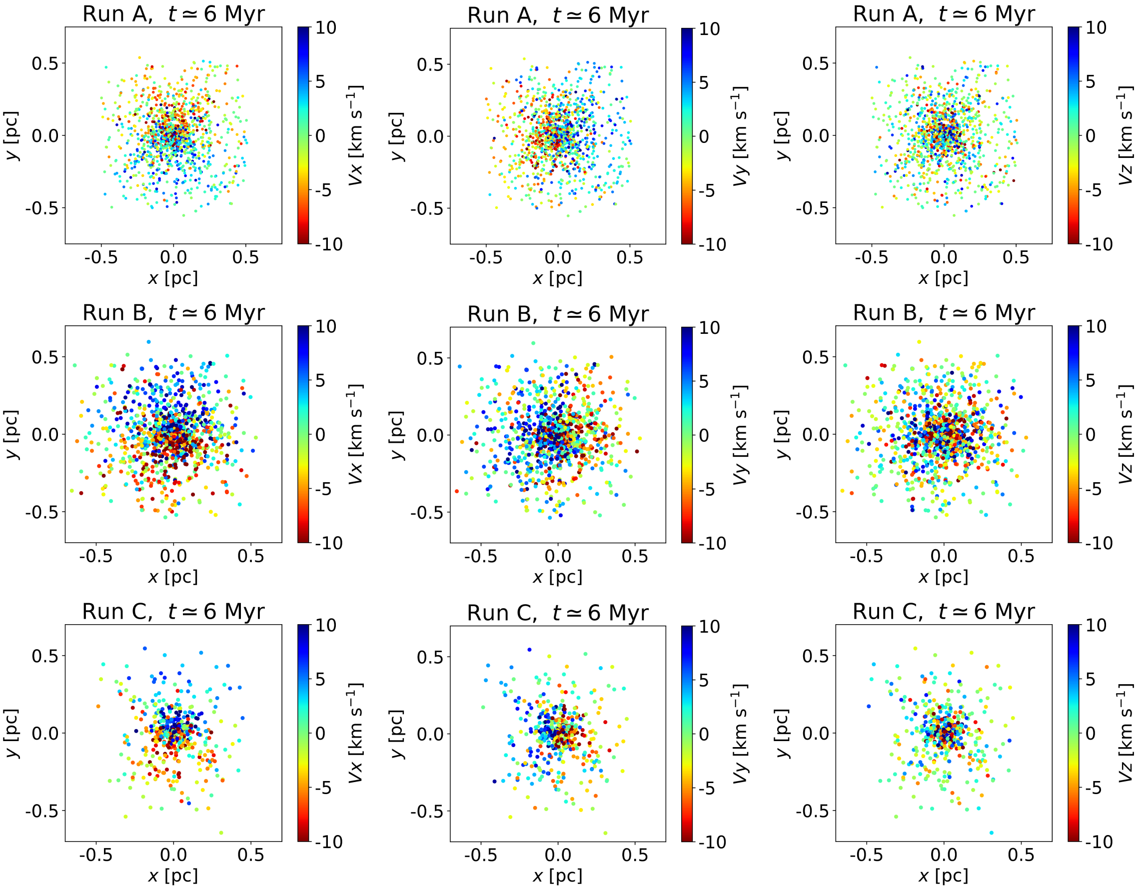

Figure 4.5: Simulated star particles (i.e. sink particles) in the xy plane at $t = 6\,\mathrm{Myr}$. The xy plane is defined as the plane perpendicular to the total angular momentum vector. From left to right: the colour-coded map shows the component of the stellar velocity along the x, y, and z axis (where the z axis is the direction of the angular momentum vector), respectively. From top to bottom: run A, B, and C.

Table 4.2: Column 1: run name; column 2: time elapsed since the beginning of the simulation (t); column 3: total SC mass (M_*); column 4: average of the absolute value of the velocity along the x-axis ($\langle|v_x|\rangle = \sum_i |v_x(i)|/N$), where $v_x(i)$ is the velocity along the x-axis of the i-th star and N is the number of stars in the SC; column 5: velocity dispersion along the x-axis ($\sigma_x = \sqrt{(N-1)^{-1}\sum_i(v_x(i) - \langle v_x\rangle)^2}$, where $\langle v_x\rangle = \sum_i v_x(i)/N$); column 6: average of the absolute value of the velocity along the x-axis over velocity dispersion along the x-axis ($\langle|v_x|\rangle/\sigma_x$).

Run	t [Myr]	M_* [$M_\odot$]	$\langle\lvert v_x\rvert\rangle$ [$\mathrm{km\,s^{-1}}$]	σ_x [$\mathrm{km\,s^{-1}}$]	$\langle\lvert v_x\rvert\rangle/\sigma_x$
A	2.5	865	5.7	6.9	0.82
A	4.0	7968	6.9	8.9	0.77
A	6.0	5759	4.2	5.9	0.70
A	9.0	5285	3.3	4.8	0.69
A	13.0	4883	3.2	4.7	0.67
B	2.5	1060	5.5	6.5	0.85
B	4.0	11874	8.6	11.8	0.73
B	6.0	9786	9.2	12.9	0.71
B	9.0	8610	9.0	12.9	0.70
B	13.0	7880	8.3	12.1	0.68
B	22.0	5975	8.1	12.2	0.67
C	2.5	202	2.2	2.9	0.77
C	4.0	2057	3.8	5.0	0.76
C	6.0	5684	8.2	11.3	0.72
C	9.0	4670	7.3	10.4	0.70
C	13.0	3911	7.7	11.1	0.69

should be absent. For my systems $t_{rh} = 3 - 7\,\mathrm{Myr}$. Since I evolved my SCs with a direct summation N-body code, I can study how dynamical evolution affects rotation. To do so, I produced many rotation curves at different timesteps, which are compared in Figure 4.6. Surprisingly, at $t = 13\,\mathrm{Myr}$ (and even at $t = 22\,\mathrm{Myr}$) SCs still show rotation. Considering that the main cluster assembled between $t = 2\,\mathrm{Myr}$ and $t = 4\,\mathrm{Myr}$, we can say that rotation persists even if $t > t_{rh}$. Rotation decreases, but on a timescale which is much longer than expected. The main rotation related properties at different timesteps are reported in Table 4.2.

This analysis may help us to put some constraints on the formation scenario of SCs. We still do not know how SCs form, but if they form through the hierarchical scenario they should rotate. The feature of rotation is thus an observational test for hierarchical assembly. This may be the case of R136, whose rotation curves are reported in Figure 4.7. R136 is the youngest massive cluster in which rotation has been observed (Hénault-Brunet et al. (2012)). It has an age of $\sim 1.5\,\mathrm{Myr}$, it rotates with velocity $v_{\mathrm{rot}} \simeq 3 \pm 1\,\mathrm{km\,s^{-1}}$ and has a ratio between rotational velocity and velocity dispersion of $v_{\mathrm{rot}}/\sigma \simeq 0.6 \pm 0.3$. These values are consistent with my simulations, even if R136 is

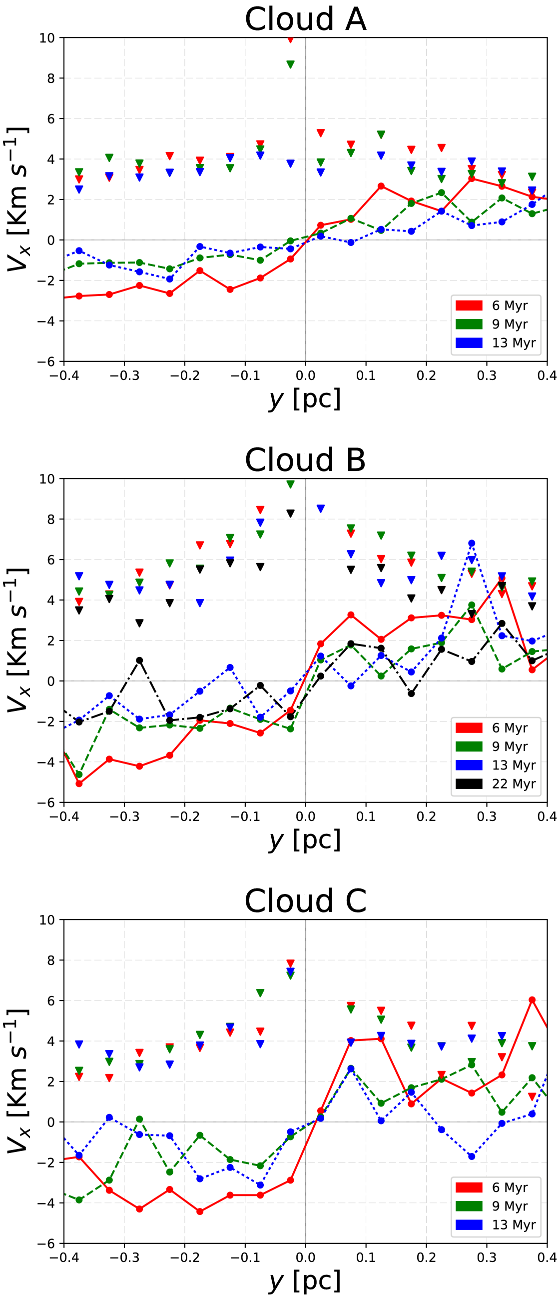

Figure 4.6: Rotation curves of the simulated SCs at different timesteps (Red: $t = 6\,\mathrm{Myr}$; green: $t = 9\,\mathrm{Myr}$; blue: $t = 13\,\mathrm{Myr}$; black: $t = 22\,\mathrm{Myr}$). Circles ($\widetilde{v}_x(y)$): average one-dimensional stellar velocity along the x-axis as a function of the position on the y axis. The values of $\widetilde{v}_x(y)$ are averaged over stars with position $y - \Delta y/2 \leq y_i \leq y + \Delta y/2$ (where y and Δy are the middle point and size of the bin, respectively). Triangles ($\sigma_x(y)$): one-dimensional stellar velocity dispersion along the x-axis as a function of the position on the y-axis. The values of $\sigma_x(y)$ are calculated as the standard deviation relative to $\widetilde{v}_x(y)$. From top to bottom: run A, B, and C.
In all runs, rotation decreases on a quite long timescale.

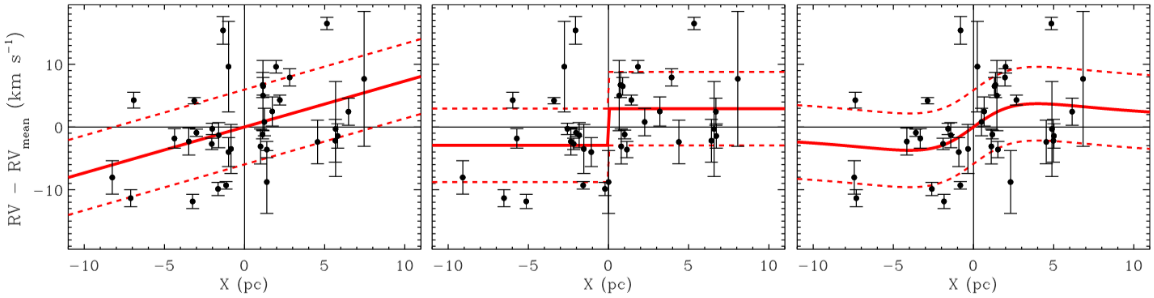

Figure 4.7: Rotational velocities of the stars in R136 as a function of distance X from the optimal rotation axis for models with constant rotation rate (left), constant rotational velocity (centre) and a more realistic rotation curve (right). The best-fit rotation curves are shown as solid red lines, and $\pm\sigma$ envelopes are represented by dashed red lines. The rotation curves are similar to those of my simulated SCs. Figure from Hénault-Brunet et al. (2012).

more massive ($M \simeq 10^5\,\mathrm{M}_\odot$ - Andersen et al. (2009)) and less compact than my SCs. Moreover, the sample of Hénault-Brunet et al. (2012) consists of only 36 O-type stars, of which only 16 are within 5 pc. Future integral field spectroscopy (e.g. HARMONI at E-ELT) and multi-conjugated adaptive optics infrared astrometry (e.g. MAORY and MICADO at E-ELT) will hopefully give us more detailed data on R136 and spot rotation signatures in other young clusters.
My results might also be useful to interpret the origin of rotation in the old GCs of the Milky Way, but it must be kept in mind that my simulated star clusters are extremely different from GCs, which are more massive and have different star formation history and age. I have evolved my systems for only ~ 20 Myr, but the fact that rotation decreases on such a long timescale might tell us that it may survive for times comparable to the age of GCs, whose rotation may have the same origin of the one which arises in my simulations.

The forthcoming analysis of cloud D will help to clear some of these doubts.

4.5 Ellipticity

The ellipticity (ϵ) allows us to quantify the flattening of SCs. To estimate the ellipticity, it is necessary to calculate the rotational inertia matrix of sink particles with respect to their centre of gravity:

$$I_{\rm rot} = \sum_i m_i \begin{bmatrix} x_i^2 & x_i y_i & x_i z_i \\ x_i y_i & y_i^2 & y_i z_i \\ x_i z_i & y_i z_i & z_i^2 \end{bmatrix}, \tag{4.4}$$

where i is the index of sink particles. The three eigenvalues of this matrix (λ_1, λ_2, λ_3) give the SC size in three orthogonal directions:

$$r_i = \beta\sqrt{\frac{5\lambda_i}{M_*}},\ i = 1, 2, 3, \tag{4.5}$$

Table 4.3: Column 1: run name; column 2: time elapsed since the beginning of the simulation (t); column 3, 4, 5: star cluster size in three orthogonal directions (r_1, r_2, r_3) obtained through the rotational inertia matrix and using a value of $\beta = 1$ in equation 4.5; column 6: star cluster ellipticity (ϵ). The larger size of the SC of run A at $t = 6\,\mathrm{Myr}$ is the consequence of an ongoing accretion of a subcluster.

Run	t [Myr]	r_1 [pc]	r_2 [pc]	r_3 [pc]	ϵ
A	2.5	0.037	0.022	0.009	0.75
A	4.0	0.55	0.39	0.32	0.42
A	6.0	1.83	3.12	2.66	0.41
A	9.0	0.61	0.55	0.45	0.27
A	13.0	0.64	0.73	0.76	0.17
B	2.5	0.024	0.013	0.007	0.71
B	4.0	0.70	0.35	0.33	0.53
B	6.0	0.28	0.26	0.25	0.1
B	9.0	0.30	0.28	0.29	0.06
B	13.0	0.48	0.33	0.33	0.32
B	22.0	0.34	0.29	0.30	0.14
C	2.5	0.018	0.011	0.004	0.75
C	4.0	0.65	0.47	0.40	0.39
C	6.0	0.25	0.21	0.20	0.20
C	9.0	0.29	0.27	0.24	0.15
C	13.0	0.29	0.25	0.24	0.16

where M_* is the total mass of sinks. The factor 5 comes from the assumption that the sink mass is uniformly distributed in space, and a correctional factor $\beta \geq 1$ accounts for the fact that the mass distribution might not be uniform but rather centrally concentrated (Lee & Hennebelle (2016)).

Ellipticity is defined as $\epsilon = 1 - \sqrt{\lambda_3/\lambda_1}$, where λ_1 and λ_3 are the maximum and minimum eigenvalue, respectively. $\epsilon = 0$ means that the SC is spherical, while $\epsilon \sim 1$ means that the SC is a disk. The SCs in my simulations are extremely flattened during the early stages of their assembly ($\epsilon \sim 0.71 - 0.75$ at $t = 2.5\,\mathrm{Myr}$). Their ellipticity diminishes over time, as shown in Figure 4.8 and in Table 4.3. At $t = 13\,\mathrm{Myr}$, my SCs are nearly spherical. The main process that makes ellipticity decrease over time is two-body relaxation. Two-body encounters change the directions of stellar velocities, which thus leave their initial preferential plane. Another possible explanation for the loss of flattening is the accretion of new gas and stellar clumps, with a different orientation of angular momentum.

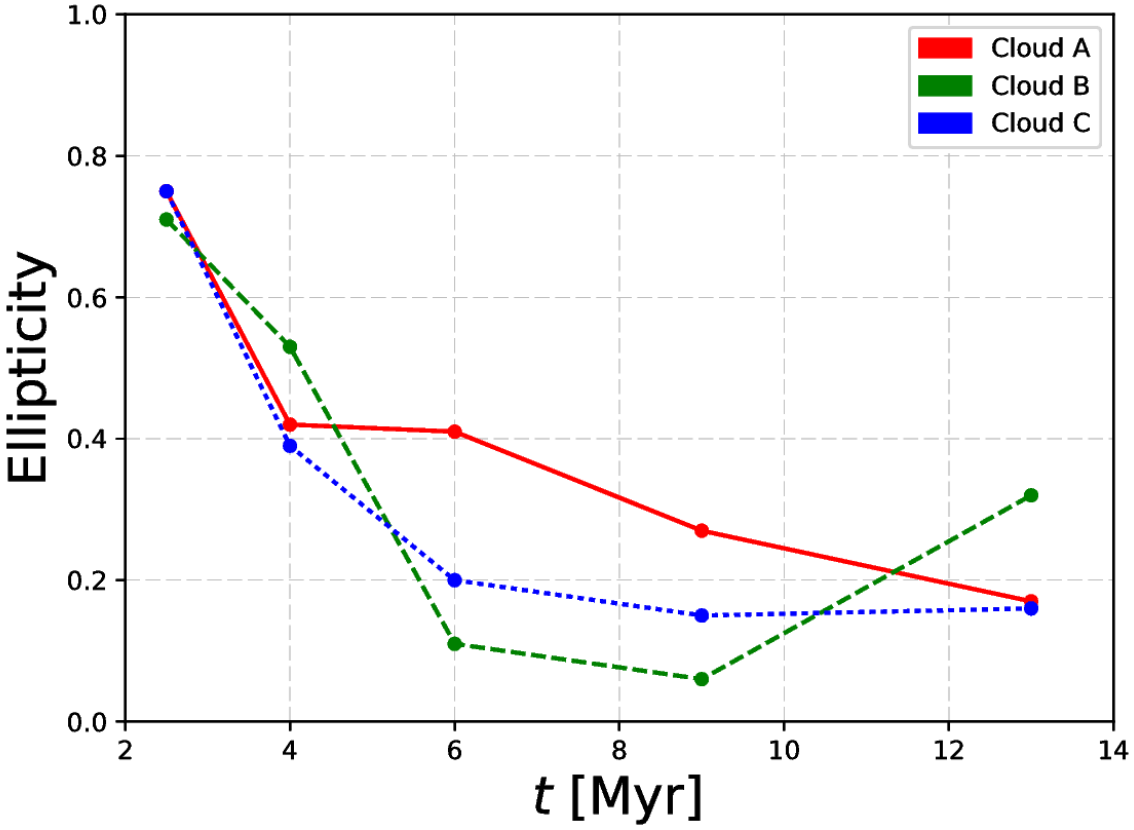

Figure 4.8: Evolution of ellipticity ϵ of simulated SCs. The red, green and blue lines represent run A, B and C respectively. All SCs are extremely flattened at the beginning, but become nearly spherical at the end of my simulations.

Chapter 5

Conclusions

In this thesis I studied the formation and kinematical features of embedded star clusters, focusing on their rotation.

I started from smoothed-particle hydrodynamics simulations of turbulence-supported molecular clouds and studied the dynamics of the main cluster that forms in each cloud using HiGPUs, a direct summation N-body code.
My star clusters form following the hierarchical assembly scenario, by the merger of several gas and stellar clumps. During this process torque is exerted on the parent gas and the stellar component, because they accrete on the main cluster structure with non-zero angular momentum. This angular momentum is transferred to the main cluster, which acquires significant rotation. In all the simulated star clusters, rotation decreases on a surprisingly long timescale ($\langle|v_x|\rangle/\sigma_x = 0.77 - 0.82$ at $t = 2.5\,\mathrm{Myr}$ and $\langle|v_x|\rangle/\sigma_x = 0.67 - 0.69$ at $t = 13.0\,\mathrm{Myr}$). My star clusters form with large ellipticity ($\epsilon = 0.71 - 0.75$ at $t = 2.5\,\mathrm{Myr}$), but they become nearly spherical through their evolution ($\epsilon = 0.14 - 0.17$ at $t = 13.0\,\mathrm{Myr}$). In particular, I found that two-body relaxation (and stellar dynamics in general) are much less effective than expected in removing angular momentum from rotating star clusters and in decreasing their ellipticity. A possible interpretation of this result could be that in a rotating system two-body encounters should be more likely on the plane of rotation, thus they should be less efficient in randomizing the directions of stellar velocities.
This work is useful to interpret the observed rotation signature in young massive clusters and in globular clusters, and it provides a key observational test for the hierarchical assembly scenario. Furthermore, my results give useful information about the initial conditions of star clusters for direct N-body simulations.

Since the study of rotation in SCs is a relatively unexplored field from the theoretical point of view, this work can be improved and further developed in many ways.
A more massive molecular cloud is currently being simulated to match the mass of the rotating young massive cluster R136. The systems could be evolved for longer times, to check how long the rotation signature lasts and to address some questions related to the origin of rotation in globular clusters. Different codes can be used to verify that the obtained results are not connected with numerical recipes. Using a population synthesis code in combination with a direct N-body code would allow to investigate how stellar evolution influences rotation. Li et al. (2017) claim that molecular clouds can

also be rotation-supported objects, so it can be useful to investigate the evolution of a globally rotating molecular cloud. Finally, the effects of a galactic external gravitational potential and a magnetic field can be studied by adding them in the simulations.

Bibliography

Hénault-Brunet, V., Gieles, M., Evans, C. J., et al. 2012, AAP, 545, L1

Portegies Zwart, S., Ishiyama, T., Groen, D., et al. 2010, IEEE Computer, v.43, No.8, p.63-70, 43, 63

Lada, C. J., & Lada, E. A. 2003, ARAA, 41, 57

Larson, R. B. 1981, MNRAS, 194, 809

Bertoldi, F., & McKee, C. F. 1992, APJ, 395, 140

Schneider, N., Csengeri, T., Hennemann, M., et al. 2012, AAP, 540, L11

Banerjee, S., & Kroupa, P. 2015, MNRAS, 447, 728

Bonnell, I. A., Bate, M. R., & Vine, S. G. 2003, MNRAS, 343, 413

Mapelli, M. 2017, MNRAS, 467, 3255

Spitzer, L. 1987, Princeton, NJ, Princeton University Press, 1987, 191 p.,

Elson, R., Hut, P., & Inagaki, S. 1987, ARAA, 25, 565

Pryor, C., Hartwick, F. D. A., McClure, R. D., Fletcher, J. M., & Kormendy, J. 1986, AJ, 91, 546

van Leeuwen, F., Le Poole, R. S., Reijns, R. A., Freeman, K. C., & de Zeeuw, P. T. 2000, AAP, 360, 472

Anderson, J., & King, I. R. 2003, AJ, 126, 772

Pancino, E., Galfo, A., Ferraro, F. R., & Bellazzini, M. 2007, APJL, 661, L155

Anderson, J., & van der Marel, R. P. 2010, APJ, 710, 1032

Bellazzini, M., Bragaglia, A., Carretta, E., et al. 2012, AAP, 538, A18

Bianchini, P., Varri, A. L., Bertin, G., & Zocchi, A. 2013, APJ, 772, 67

Fabricius, M. H., Noyola, E., Rukdee, S., et al. 2014, APJL, 787, L26

Kimmig, B., Seth, A., Ivans, I. I., et al. 2015, AJ, 149, 53

Lardo, C., Pancino, E., Bellazzini, M., et al. 2015, AAP, 573, A115

Lee, J.-W. 2015, APJS, 219, 7

Davies, B., Bastian, N., Gieles, M., et al. 2011, MNRAS, 411, 1386

Mackey, A. D., Da Costa, G. S., Ferguson, A. M. N., & Yong, D. 2013, APJ, 762, 65

Li, G.-X., Wyrowski, F., & Menten, K. 2017, AAP, 598, A96

Vesperini, E., Varri, A. L., McMillan, S. L. W., & Zepf, S. E. 2014, MNRAS, 443, L79

Gavagnin, E., Mapelli, M., & Lake, G. 2016, MNRAS, 461, 1276

Wadsley, J. W., Stadel, J., & Quinn, T. 2004, NA, 9, 137

Hernquist, L., & Katz, N. 1989, APJS, 70, 419

Stadel, J. G. 2001, Ph.D. Thesis, 3657

Barnes, J., & Hut, P. 1986, Nature, 324, 446

Sutherland, R. S., & Dopita, M. A. 1993, APJS, 88, 253

Boley, A. C. 2009, APJL, 695, L53

Boley, A. C., Hayfield, T., Mayer, L., & Durisen, R. H. 2010, Icarus, 207, 509

D'Alessio, P., Calvet, N., & Hartmann, L. 2001, APJ, 553, 321

Quinn, T., Katz, N., Stadel, J., & Lake, G. 1997, arXiv:astro-ph/9710043

Capuzzo-Dolcetta, R., Spera, M., & Punzo, D. 2012

Nitadori, K., & Makino, J. 2008, NA, 13, 498

Plummer, H. C. 1911, MNRAS, 71, 460

Gaburov, E., Harfst, S., & Portegies Zwart, S. 2009, NA, 14, 630

Bate, M. R., Bonnell, I. A., & Bromm, V. 2003, MNRAS, 339, 577

King, I. R. 1966, AJ, 71, 64

Proszkow, E.-M., Adams, F. C., Hartmann, L. W., & Tobin, J. J. 2009, APJ, 697, 1020

Andersen, M., Zinnecker, H., Moneti, A., et al. 2009, APJ, 707, 1347

Lee, Y.-N., & Hennebelle, P. 2016, AAP, 591, A30

Galli, D., Lizano, S., Shu, F. H., & Allen, A. 2006, APJ, 647, 374

Acknowledgements

Ringrazio Michela Mapelli per esser stata la mia supervisor, ma soprattutto per gli insegnamenti, per la fiducia, gli incoraggiamenti e per avermi aiutato a trovare un futuro nel mondo astrofisico.
Grazie anche a Mario Spera per avermi insegnato ad utilizzare il suo codice, per la disponibilità e per le mille lettere di referenza.
Grazie alla mia famiglia, a SB e ad i miei più cari amici per aver reso tutto più semplice e sereno, per avermi aiutato a superare i momenti più brutti in cui avrei altrimenti mollato tutto.
Lascio Padova dopo tanti anni con un "ocean of sorrow in me". Sono sicuro che i legami più forti e sinceri rimarranno tali.

"And although I wish
that I could stay
it somehow strangely feels ok.
It is what it is,
I'll find my way
through this passing light..."